

Flow-acoustic resonance in deep and inclined cavities

You Wei Ho^{1*} and Jae Wook Kim²

¹ *Institute of Sound & Vibration Research, University of Southampton, Southampton, SO17 1BJ, United Kingdom*

² *Aeronautics & Astronautics, University of Southampton, Southampton, SO17 1BJ, United Kingdom*

(Dated: July 11, 2024)

This paper presents numerical investigations of flow-acoustic resonances in deep and inclined cavities using wall-resolved large eddy simulations. The study focuses on cavity configurations with an aspect ratio of $D/L = 2.632$, subjected to two Mach numbers of 0.2 and 0.3 at three different inclination angles ($\alpha = 30^\circ$, 60° , and 90°). Fully turbulent boundary layers generated from independent precursor simulations are employed upstream of the cavities. Initial results highlight distinct aeroacoustic responses between inclined and orthogonal cavities, particularly at $M_\infty = 0.3$, where inclined cavities exhibit stronger resonances at a lower peak frequency ($St \approx 0.27$) compared to the orthogonal cavity. Further analysis reveals that this lower Strouhal number corresponds to a reduced vortex convection speed linked to large shear-layer oscillations. Additionally, the acoustic input-output analysis indicates that the inclined cavities amplify acoustic responses more effectively and exhibit weaker source-sink cancellations compared to the orthogonal cavity. These mechanisms are identified as the primary contributors to the enhanced aeroacoustic responses in the inclined cavities. Finally, this paper proposes that the ratio between acoustic particle displacement and momentum thickness may be used as a criterion to predict the onset of the distinctive resonance at $St \approx 0.27$. It is suggested that the amplified resonances may be linked to a nonlinear mode shift of the first hydrodynamic mode through enhanced shear-layer oscillation taking place when the proposed criterion is met.

I. INTRODUCTION

Flow-acoustic resonances arising from aeroacoustic instabilities in deep cavity flows generate high-intensity pressure waves with discrete frequencies, leading to adverse effects such as noise pollution and structural fatigue in various engineering applications, including safety valves [1, 2], closed side-branches in gas transport systems [3, 4], turbomachinery [5, 6], and riverine environments [7]. The origin of these flow-acoustic resonances is intricately linked to the complex interplay between hydrodynamic and resonant acoustic fields [3, 8]. Specifically, when airflow passes over a deep cavity under certain conditions, such as specific speeds, angles of flow, or cavity geometries, it can initiate self-sustained oscillations that couple with an acoustic mode and generate intense aerodynamic noise. In this process, acoustic resonance plays an important role in serving as the primary feedback mechanism that amplifies oscillations and induces flow tone lock-ins [9]. This phenomenon is fundamentally different from oscillations in shallow cavities, which are predominantly governed by the Rossiter feedback mechanism that facilitates upstream acoustic feedback [10, 11]. Consequently, the need to better understand the distinct underlying physical mechanisms driving these deep cavity oscillations merits special attention.

The aeroacoustics of deep cavity flows have received considerable attention in the scientific literature. Previous notable studies by [10, 12–14] have provided substantial evidence that deep cavity flows generate pronounced acoustic responses near depthwise acoustic modes. Rockwell and Naudascher [15] termed this phenomenon “fluid resonant oscillation,” which arises from the interaction between the excitation of the shear-layer oscillation and the reinforcement provided by the depthwise acoustic resonances. According to their studies, fluid resonant oscillation originates with initial shear-layer instabilities near the upstream separation corner, generating acoustic standing waves within the cavity upon interaction with the downstream corner. The resulting resonant acoustic field induces velocity perturbations, which, in turn, amplify the instabilities within the shear-layer and close the feedback loop. This feedback loop is particularly significant in deep cavity systems due to their susceptibility to depthwise acoustic modes that exhibit minimal radiation losses [16]. Consequently, the induced velocity perturbations by these acoustic resonances may further instigate the instabilities within the shear-layer, ultimately leading to the formation of the highly coherent vortex structures observed in deep cavity flows [17–20].

The phenomenon of flow-acoustic resonances in deep cavities typically occurs within specific ranges of the Strouhal number, each corresponding to a distinct hydrodynamic mode of the flow field. These hydrodynamic modes are characterized by the number of convecting vortex structures across the cavity opening that satisfy the requisite

* Corresponding author: ywh1g14@soton.ac.uk

streamwise phase criterion [21–23]. It is widely observed that flow-acoustic resonances in deep cavities, triggered by the first hydrodynamic mode, yield significantly stronger acoustic responses at a Strouhal number of approximately $St \approx 0.4$ [18]. Conversely, flow-acoustic resonances excited by higher hydrodynamic modes, although generally weaker, have also been reported at Strouhal numbers exceeding $St \approx 0.8$ [9, 18]. However, recent experimental studies on closed side-branches have revealed an additional category of flow-acoustic resonance occurring at a lower Strouhal number, $St \approx 0.27$, characterized by acoustic responses that surpass the dynamic pressure of the flow [8, 9, 24–26]. Moreover, it has been observed that the resonant acoustic field exerts a substantial influence on the coherence and trajectory of the vortex structure within this resonance regime. According to Peters [8], the resulting amplification of instabilities and intense shear-layer oscillations transition into highly nonlinear states, posing significant challenges in accurately describing the fluid resonant mechanism. Consequently, despite considerable empirical evidence, an in-depth quantitative analysis that elucidates the physical mechanisms driving these pronounced flow-acoustic resonances at $St \approx 0.27$ remains unresolved.

In recent years, modal analysis techniques, including global linear stability analysis and receptivity analysis, have emerged as powerful tools for investigating asymptotic long-time flow instabilities and elucidating the underlying mechanisms driving instability in various fluid-flow systems [27–36, 38]. The application of direct global modes and adjoint modes derived from these modal analyses has provided significant insights into the structural sensitivity within flow fields [28, 32, 37, 38]. Concurrently, non-modal approaches, such as resolvent analysis, initially introduced by Trefethen et al. [39] and later extended for turbulent mean flows by McKeon et al. [40], have become an important theoretical framework for examining energy amplification and the associated structural response to perturbations across a spectrum of frequencies in shallow and deep cavity flows [41–43]. Despite these advancements, a notable gap persists in the literature concerning the application of resolvent analysis as an acoustic input-output analysis to investigate flow-acoustic resonances in deep and inclined cavity flows. To the authors’ knowledge, the potential of employing such an input-output analysis to uncover the optimal forcing, response, and amplification of acoustic perturbations that drive flow-acoustic resonance in these specific cavity configurations remains unexplored.

Furthermore, despite significant progress in understanding the aeroacoustics of deep cavity flows, most numerical investigations to date have predominantly concentrated on orthogonal cavity geometries [44–48]. Consequently, there is currently a limited understanding of the noise generation mechanisms involving turbulent flows over deep and inclined cavities in resonance. This paper aims to bridge these knowledge gaps through detailed numerical investigations using wall-resolved large-eddy simulations (LES). Detailed numerical investigations into the distinct vortex dynamics and the noise generation process for both orthogonal and inclined cavity configurations will be presented. The primary objective of this study is to elucidate the remarkably different aeroacoustic responses of inclined cavities compared to their orthogonal counterparts. For this purpose, specific inclination angles and flow speeds have been selected to highlight these distinct aeroacoustic behaviors of inclined cavity flows. However, the mechanisms surrounding the transition of the aeroacoustic response occurring across the critical Mach number or the inclination angle are not the central focus of this paper.

This paper is structured and written in the following order. Section II introduces the computational set-up and methods used in this study. In Sections III and IV, the acoustic and hydrodynamic fields around the cavity region are investigated in detail. Section V moves the focus to examine the acoustic amplifications and source-sink cancellations through acoustic input-output analysis, where we also discuss the critical factor of the ratio of acoustic particle displacement to momentum thickness in defining the distinct resonance behaviors. Finally, concluding remarks are provided in VI.

II. DESCRIPTION OF PROBLEM AND THE COMPUTATIONAL SET-UP

The present study investigates the cavity section with a length of $L/h = 0.608$ and depth of $D/h = 1.6$, enclosed in a channel with a height of $2h$, as shown in figure 1. The Reynolds number based on the cavity opening length, $L = 0.038$ m, is set to $Re_\infty = 261,891$ and a freestream Mach number of $M_\infty = 0.3$ based on the ambient speed of sound (for air) of $a_\infty = 340.2$ m/s and the reference temperature of $T_\infty = 288$ K are also considered in this work. The current numerical investigation employs a high-resolution implicit large-eddy simulation (ILES) method based on a wavenumber-optimized discrete filter [49]. The filter is applied directly to the solution (conservative variables) at every time step and acts as an implicit sub-grid scale (SGS) model that enforces the dissipation of scales smaller than the filter cutoff wavelength. Garmann et al. [50] performed an extensive analysis of the ILES technique compared to the traditional implementation of an explicit SGS model and concluded that ILES simulations can correctly capture the flow physics when the grid is subjected to an appropriate resolution.

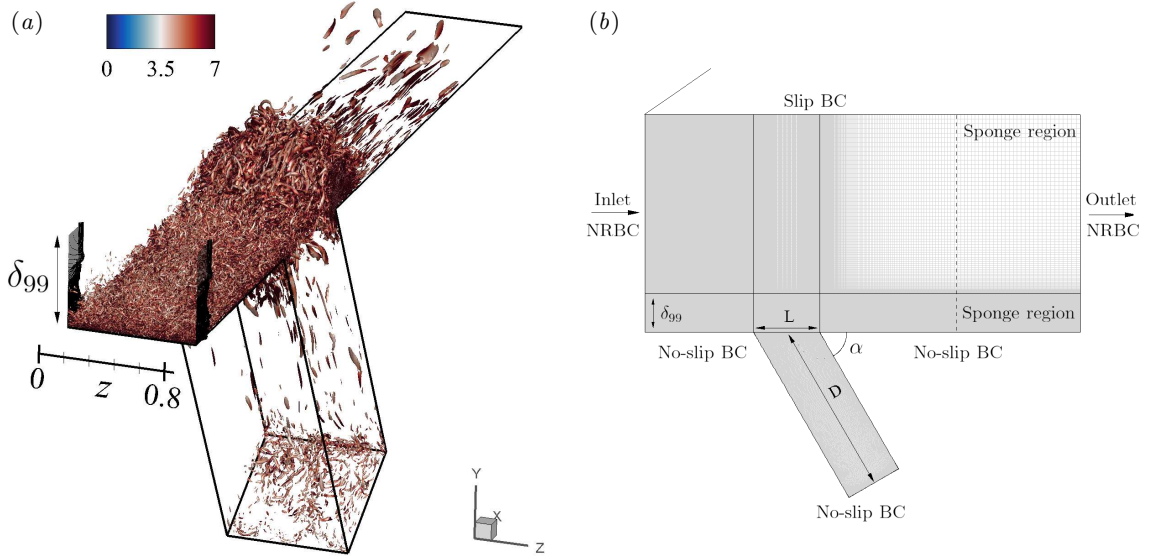


FIG. 1. Visualizations of the current computational domain of the deep and inclined cavity configuration enclosed in a channel. (a) Instantaneous non-dimensional Q -criterion iso-surfaces ($Q = 5$) coloured by non-dimensional vorticity magnitude ($|\omega_i|$), unveiling three-dimensional vortices within the turbulent boundary layer. (b) A spanwise view of the computational domain used in the current numerical investigation. The cavity length and depth are denoted by L and D , respectively.

A. Governing equations and numerical methods

In this work, the full 3-D compressible Navier-Stokes equations (with a source term for sponge layers included) are used, which can be expressed in a conservative form, transformed onto a generalised coordinate system as

$$\frac{\partial}{\partial t} \left(\frac{\mathbf{Q}}{J} \right) + \frac{\partial}{\partial \xi_i} \left(\frac{\mathbf{E}_j - Re_\infty^{-1} M_\infty \mathbf{F}_j}{J} \frac{\partial \xi_i}{\partial x_j} \right) = - \frac{a_\infty}{L} \frac{\mathbf{S}}{J}, \quad (1)$$

where the indices $i = 1, 2, 3$ and $j = 1, 2, 3$ denote the three dimensions. The vectors of the conservative variables, inviscid and viscous fluxes, are given by

$$\left. \begin{aligned} \mathbf{Q} &= [\rho, \rho u, \rho v, \rho w, \rho e_t]^T, \\ \mathbf{E}_j &= [\rho u_j, (\rho u u_j + \delta_{1j} p), (\rho v u_j + \delta_{2j} p), (\rho w u_j + \delta_{3j} p), (\rho e_t + p) u_j]^T, \\ \mathbf{F}_j &= [0, \tau_{1j}, \tau_{2j}, \tau_{3j}, u_i \tau_{ji} + q_j]^T, \end{aligned} \right\} \quad (2)$$

with the stress tensor and heat flux vector written as

$$\tau_{ij} = \mu \left(\frac{\partial u_i}{\partial x_j} + \frac{\partial u_j}{\partial x_i} - \frac{2}{3} \delta_{ij} \frac{\partial u_i}{\partial x_i} \right), \quad q_j = \frac{\mu}{(\gamma - 1) Pr} \frac{\partial T}{\partial x_j}, \quad (3)$$

where $\xi_i = \{\xi, \eta, \zeta\}$ are the generalised coordinates, $x_j = \{x, y, z\}$ are the Cartesian coordinates, δ_{ij} is the Kronecker delta, $u_j = \{u, v, w\}$, $e_t = p/[(\gamma - 1)\rho] + u_j u_j / 2$ and $\gamma = 1.4$ for air. The local dynamic viscosity μ is calculated by using Sutherland's law [51]. In the current set-up, ξ , η and ζ are aligned in the streamwise, vertical and spanwise directions, respectively. The Jacobian determinant of the coordinate transformation (from Cartesian to the generalised) is given by $J^{-1} = |\partial(x, y, z)/\partial(\xi, \eta, \zeta)|$ [52]. The extra source term \mathbf{S} on the right-hand side of (1) is non-zero within the sponge layer only, which is described in Kim *et al.* [53, 54]. In this paper, the freestream Mach and Reynolds numbers are defined as $M_\infty = U_\infty / a_\infty$ and $Re_\infty = \rho_\infty U_\infty L / \mu_\infty$ where $a_\infty = \sqrt{\gamma p_\infty / \rho_\infty}$ is the ambient speed of sound and $U_\infty = \sqrt{u_\infty^2 + v_\infty^2 + w_\infty^2}$ is the speed of the freestream mean flow. The governing equations are non-dimensionalised based on the streamwise cavity opening length $L = 38$ mm for length scales, the ambient speed of sound a_∞ for velocities, L/a_∞ for time scales and $\rho_\infty a_\infty^2$ for pressure, unless otherwise notified. Temperature, density and dynamic viscosity are normalised by their respective ambient values: T_∞ , ρ_∞ and μ_∞ .

The governing equations given above are solved using high-order accurate numerical methods specifically developed for aeroacoustic simulation on structured grids. The flux derivatives in space are calculated based on fourth-order

pentadiagonal compact finite difference schemes with seven-point stencils [55]. Explicit time advancing of the numerical solution is carried out using the classical fourth-order Runge-Kutta scheme with a CFL number of 0.95. Numerical stability is maintained by implementing sixth-order pentadiagonal compact filters for which the cutoff wavenumber (normalized by the grid spacing) is set to 0.85π . In addition to the sponge layers used, characteristics-based non-reflecting boundary conditions (NRBC) based on [56] are applied at the inflow and outflow boundaries to prevent any outgoing waves from returning to the computational domain. Periodic conditions are used across the spanwise boundary planes unless otherwise stated. Slip (no penetration) and no-slip wall boundary conditions based on [57] are applied at the top and bottom channel walls, respectively.

The computation is parallelized via domain decomposition and message passing interface (MPI) approaches. The compact finite difference schemes and filters used are implicit in space due to the inversion of pentadiagonal matrices involved, which requires a precise and efficient technique for parallelization to avoid numerical artifacts that may appear at the subdomain boundaries. A recent parallelization approach based on quasi-disjoint matrix systems [58] offering super-linear scalability is used in the present paper.

B. Simulation set-up and discretisation of the problem

The cavity geometry and the computational domain used in this work comprises $x/L \in [-1.64, 4.93]$ in the streamwise direction, $y \in [-2.63, 3.29]$ in the vertical direction and $z/L \in [0, 0.822]$ in the spanwise direction. The entire computational domain; the inner region (physical domain) where meaningful simulation data are obtained; and, the sponge layer zone is defined as

$$\left. \begin{aligned} \mathcal{D}_\infty &= \{\mathbf{x} \mid x/L \in [-1.644, 4.934], y \in [-2.632, 3.289], z/L \in [0, 0.822]\}, \\ \mathcal{D}_{\text{physical}} &= \{\mathbf{x} \mid x/L \in [-1.644, 3.289], y \in [-2.632, 3.289], z/L \in [0, 0.822]\}, \\ \mathcal{D}_{\text{sponge}} &= \mathcal{D}_\infty - \mathcal{D}_{\text{physical}}. \end{aligned} \right\} \quad (4)$$

The physical domain, \mathcal{D}_∞ consists of a deep cavity with an aspect ratio of $D/L = 2.632$ enclosed in a straight rectangular channel with a channel half-height of $h/L = 1.644$. The channel region is discretised by $960 \times 290 \times 480$ grid points in streamwise, vertical, and spanwise directions. A total of $240 \times 240 \times 480$ grid points are used in the streamwise, vertical and spanwise directions, respectively, in the cavity region. The mesh in the wall-normal direction is refined close to the viscous wall $y^+ \approx 1$ to maintain a sufficiently high level of near-wall grid resolution throughout the viscous wall surfaces.

Re_∞	M_∞	δ_{99}/L	δ^*/L	θ/L	H
261,891	0.3	0.388	0.037	0.030	1.23

TABLE I. Boundary layer parameters used as the inflow condition for the current cavity simulations.

The inlet is located at $x/L = -1.664$ upstream of the cavity, where the turbulent inflow data is injected. The outflow boundary is placed at a relatively remote location downstream from the cavity, allowing a sufficient distance for the vortices to dissipate. A precursor simulation is employed to generate the prerequisite turbulent inflow data for the cavity simulation. The precursor simulation domain size ($L_x \times L_y \times L_z$) was set to $4\delta_{99} \times 1\delta_{99} \times 2\delta_{99}$ with $480 \times 240 \times 480$ grid points in the streamwise, vertical and spanwise directions, respectively. The initial boundary layer thickness, δ_{99} is determined analytically based on Na and Lu [59], and the channel flow is initialised with the turbulent mean flow profile according to Spalding [60]. Periodic boundary conditions are applied in streamwise and spanwise directions, and a streamwise pressure gradient is applied to maintain the desired mass flow rate. The precursor simulation is completed when the mean flow profile is converged, and the obtained instantaneous flow solutions are injected into the cavity simulation through the inlet plane. Figure 2 shows a close agreement of the time-averaged turbulent velocity profile and the Reynolds stresses between the current half-channel LES and a full-channel DNS by Lozano-Durán and Jiménez [61], conducted at $Re_\tau \approx 3900$ and 4200, respectively. The inflow boundary layer information for the current simulation is listed in table I.

C. Definition of variables for statistical analysis

Data processing and analysis are performed upon the completion of the simulation. The main property required in this study is the power spectral density (PSD) function of the pressure fluctuations around the cavity. To facilitate

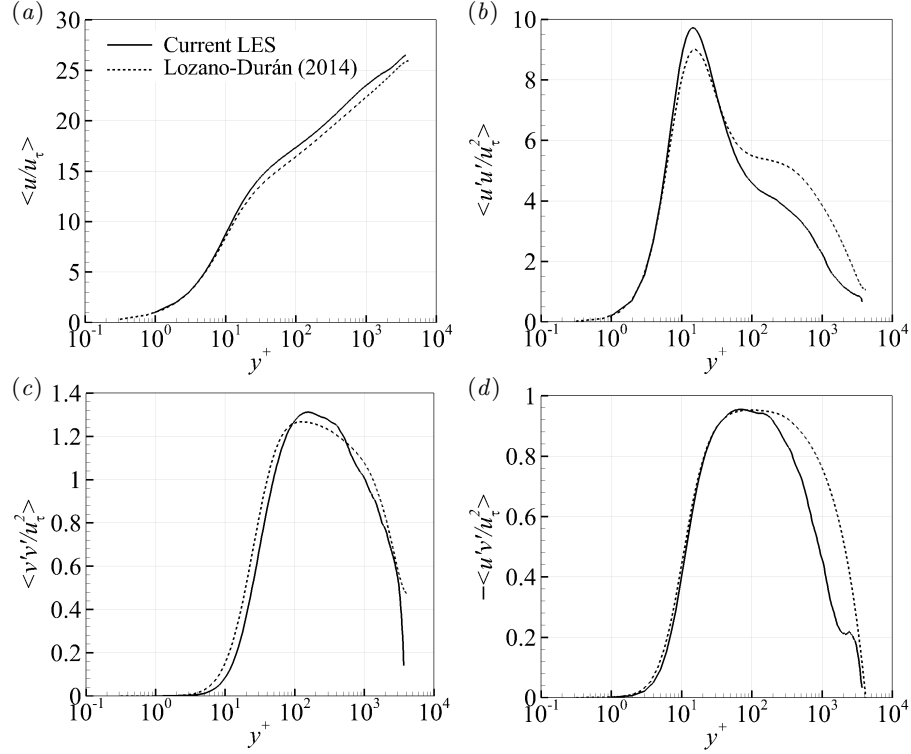


FIG. 2. (a) Time-averaged velocity profile of the turbulent boundary layer; and (b–d) Reynolds stresses obtained from the current precursor half-channel LES ($Re_\tau \approx 3900$), compared with the full-channel DNS ($Re_\tau \approx 4200$) by Lozano-Durán and Jiménez [61].

the following discussions, we defined the pressure fluctuations here as

$$p'(\mathbf{x}, t) = p(\mathbf{x}, t) - \bar{p}(\mathbf{x}), \quad (5)$$

where $\bar{p}(\mathbf{x})$ is the time-averaged pressure field. Following the definitions used in Goldstein [62], the PSD functions of the pressure fluctuations (based on frequency and one-sided) are then calculated by

$$S_{pp}(\mathbf{x}, f) = \lim_{T \rightarrow \infty} \frac{\hat{p}(\mathbf{x}, f, T) \hat{p}^*(\mathbf{x}, f, T)}{T}, \quad (6)$$

where \hat{p} is an approximate Fourier transform of p , respectively, based on the following definition:

$$\hat{p}(\mathbf{x}, f, T) = \int_{-T}^T p'(\mathbf{x}, t) e^{-2\pi i f t} dt, \quad (7)$$

and, ‘*’ denotes a complex conjugate. Similarly, the magnitude and the respective phase of the single-sided Fourier transform pressure field are calculated by

$$|p(\mathbf{x}, f, T)| = 2\sqrt{\hat{p}(\mathbf{x}, f, T) \hat{p}^*(\mathbf{x}, f, T)}, \quad (8)$$

$$\Phi_p(\mathbf{x}, f, T) = \arctan \left\{ \frac{\text{Im}[\hat{p}(\mathbf{x}, f, T)]}{\text{Re}[\hat{p}(\mathbf{x}, f, T)]} \right\}. \quad (9)$$

In the above equations, T represents the half-length of the time signals used for the approximate Fourier transform. The same procedures and notation are used for other field quantities later in this paper.

D. Acoustic input-output analysis

Recently, the Acoustic Perturbation Equations (APEs) proposed by Ewert and Schröder [63] have been successfully demonstrated as a useful hybrid approach for accurately predicting acoustic propagation within cavity flows by using

acoustic sources computed directly from fluid simulations [64, 65]. In this research, we employ APEs as a linear operator to explore the dominant acoustic input-output behavior of deep cavity systems based on the time-averaged mean flow states. To achieve this, we incorporate the APE-4 formulation, expressed as

$$\frac{\partial p'}{\partial t} + \bar{c}^2 \cdot \left(\bar{\rho} \hat{\mathbf{u}} + \bar{\mathbf{u}} \frac{\hat{p}}{\bar{c}^2} \right) = \bar{c}^2 q_e, \quad (10)$$

$$\frac{\partial \mathbf{u}'}{\partial t} + \nabla (\bar{\mathbf{u}} \cdot \hat{\mathbf{u}}) + \nabla \left(\frac{\hat{p}}{\bar{\rho}} \right) = \mathbf{q}_m, \quad (11)$$

where the noise sources are given by

$$q_c = -\nabla \cdot (\rho' u')' + \frac{\bar{\rho}}{C_p} \frac{Ds'}{Dt}, \quad (12)$$

$$\mathbf{q}_m = -(\boldsymbol{\omega} \times \mathbf{u})' + T' \nabla \hat{s} - s' \nabla \hat{T} - \left(\nabla \frac{\mathbf{u}'^2}{2} \right)' + \left(\frac{\nabla \cdot \hat{\boldsymbol{\tau}}}{\rho} \right)'. \quad (13)$$

The variables marked with a prime symbol denote fluctuating quantities, whereas those with an overbar represent time-averaged values. Among the source terms, those encapsulating two primed quantities are generally smaller than their counterparts, and consequently, their contribution to the overall sources is considered negligible and thus omitted. In addition, considering the high Reynolds number and relatively low Mach number flow discussed in this paper, the contributions of viscosity and entropy to the sources can be safely omitted. Consequently, the Lamb vector, defined as $(\boldsymbol{\omega} \times \mathbf{u})'$, is considered the dominant source term. Applying these simplifications, Eq. (10) and Eq. (11) are rewritten in a compact form, expressed as

$$\frac{\partial \mathbf{q}'}{\partial t} = \mathbf{L}(\bar{\mathbf{q}}) + \mathbf{f}', \quad (14)$$

where $\mathbf{L}(\bar{\mathbf{q}})$ denotes the linear operator about the mean flow state $\bar{\mathbf{q}} = [\bar{p}, \bar{u}, \bar{v}, \bar{w}]^T$ and \mathbf{f}' represents the forcing input comprised of the Lamb vector. Accordingly, a modal perturbation of the form

$$\mathbf{q}'(x, y, z, t) = \hat{\mathbf{q}}(x, y) \exp i(\beta z - \omega t) + \text{complex conjugate}, \quad (15)$$

is imposed to Eq. (14) to form an acoustic input-output dynamics, expressed as

$$\hat{\mathbf{q}}_\omega = [-i\omega \mathbf{I} - \mathbf{L}(\bar{\mathbf{q}})]^{-1} \hat{\mathbf{f}}_\omega = \mathbf{R}(\bar{\mathbf{q}}; \omega) \hat{\mathbf{f}}_\omega. \quad (16)$$

Here, the acoustic input-output (or acoustic resolvent) operator $\mathbf{R}(\bar{\mathbf{q}}; \omega)$ relates the input forcing (i.e., Lamb vector), $\hat{\mathbf{f}}_\omega$, to the output fields as acoustic quantities (i.e., acoustic pressure fields), $\hat{\mathbf{q}}_\omega$, in the frequency space. The complex eigenvalue is represented by $\omega = \omega_r + i\omega_i$, with the real part of the eigenvalue, ω_r , determining the physical frequency, while its imaginary component determines the radiation loss associated with the acoustic eigenmode ($\omega_i < 0$). Furthermore, the acoustic eigenmodes of the cavity systems, which may be influenced by the mean flow field [64], can be retrieved by solving the eigenvalue problem presented in the homogeneous form of Eq. (16). Accordingly, the discretized acoustic input-output operator is solved using singular value decomposition to determine the directions spanned by the forcing input and the state output vectors, such as

$$\mathbf{R}_{\bar{\mathbf{q}}, \omega} = \mathbf{U} \Sigma \mathbf{V}^*, \quad (17)$$

where $\mathbf{U} = [\hat{U}_1, \hat{U}_2, \hat{U}_3, \dots]$ and $\mathbf{V} = [\hat{V}_1, \hat{V}_2, \hat{V}_3, \dots]$ provide the leading optimal sets of responses and the corresponding forcing mode vectors. The amplification gains of the leading optimal sets are determined by the corresponding singular values $\Sigma = \text{diag}(\sigma_1, \sigma_2, \sigma_3, \dots)$, which are arranged in descending order. The superscript in Eq. (17) indicates the Hermitian transpose operation. In this study, non-penetrating boundary conditions (i.e., zero wall-normal velocity perturbation) are enforced at the wall. Additionally, non-reflecting characteristic boundary conditions introduced by Thompson [66, 67] and damping sponge regions are used in combination to minimize artificial numerical reflections. The approximation of spatial derivatives was achieved using a standard second-order finite difference scheme. Finally, the eigenvalues and eigenvectors of the linear operator were retrieved via the Krylov-Schur algorithm [68]. All eigenmodes presented in this paper achieved convergence within a tolerance level of $\|\omega \mathbf{A} \hat{\mathbf{Q}} - \mathbf{L} \hat{\mathbf{Q}}\| \leq O(10^{-14})$.

III. PRESSURE FLUCTUATIONS AND OSCILLATION FREQUENCIES

The self-sustained fluid-resonant oscillation observed in deep and inclined cavities is caused by the interaction between the shear-layer fluctuation over the cavity opening and an acoustic mode within the cavity. This interaction reinforces large-scale vortical structures, modifying the flow field and generating highly intense acoustic pressure fluctuations. The process, which efficiently converts local flow energy into acoustic energy, is visualized in figure 3.

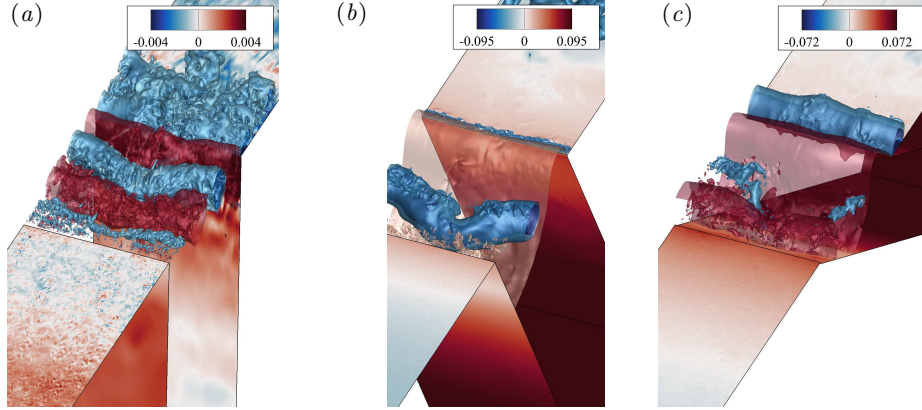


FIG. 3. The large-scale vortical structures are identified through iso-contours of instantaneous pressure fluctuations. Note that the flow direction is from left to right. The surface contours of wall-pressure fluctuations reveal the prominent acoustic field emanating from deep cavities with the inclination angles of (a) $\alpha = 90^\circ$, (b) 60° , and (c) 30° , respectively.

This section investigates the aeroacoustic behavior of wall-pressure fluctuations in deep cavities subjected to three distinct inclination angles at two specific Mach numbers, resulting in a total of six simulations. Initially, simulations are performed using a turbulent inflow dataset at a Mach number of $M_\infty = 0.3$ for four million time steps, corresponding to 220 non-dimensional time units. After this period, a steady-periodic state of the wall-pressure signal is achieved at the cavity's base across all angles of inclination, as depicted in figure 4(a). Subsequently, the Fourier transform is applied to the pressure time signals over an additional non-dimensional time span of approximately 740 samples (taken every 0.164 time unit) from the computational data, covering a total non-dimensional time of 120. This interval captures roughly ten cycles of the lowest fundamental frequency. The resulting time signals are nearly periodic, and any steady component is eliminated prior to the Fourier transform. Various windowing functions have been tested, and the results exhibit comparable spectrum compositions. Following this, the procedures are repeated using a turbulent inflow dataset at a Mach number of $M_\infty = 0.2$, as previously examined by Ho and Kim [23], and the corresponding wall-pressure signal from each inclination is presented in figure 4(b). Evidently, the time signals from inclined cavities exhibit highly periodic oscillations, underscoring the self-sustaining nature of the oscillation at both Mach numbers.

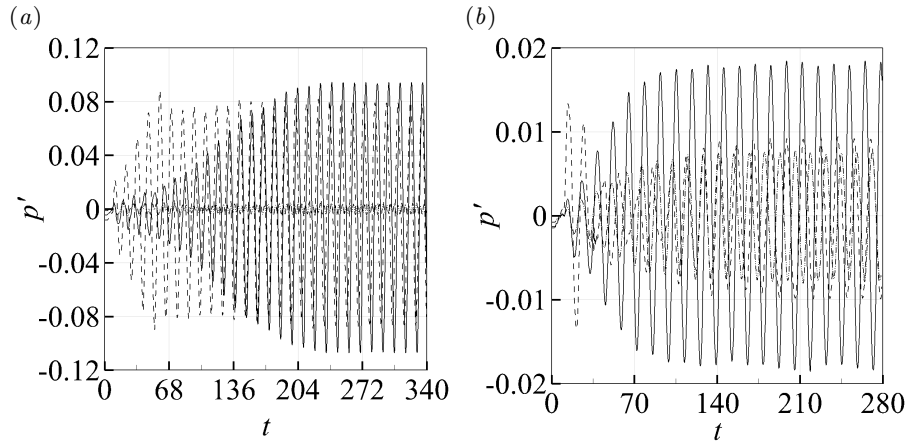


FIG. 4. The spanwise-averaged time signal of the pressure fluctuations measured on the base surface of the cavities with the inclinations: (---) $\alpha = 90^\circ$, (—) 60° , and (---) 30° at free-stream Mach numbers of (a) $M_\infty = 0.3$ and (b) $M_\infty = 0.2$, respectively.

The power spectra of wall-pressure fluctuations at $M_\infty = 0.2$ are depicted in figure 5(b). The figure shows that all three cavity cases ($\alpha = 30^\circ$, 60° , and 90°) produce a flow-acoustic resonance closely associated with the fundamental frequency ($St \approx 0.385$). The authors have previously investigated the orthogonal cavity flow characteristics at this fundamental frequency [23], where the critical Mach number for this particular cavity geometry ($D/L = 2.632$) and inflow condition ($\theta/L = 0.0345$) was estimated to be $M_\infty = 0.2$. This critical condition was understood to result from a lock-in event between the first Rossiter's streamwise feedback and depthwise acoustic resonance modes. Therefore, any deviation in flow speed from this Mach number is expected to produce a sub-optimal flow-acoustic resonance. This assumption is supported by the weaker acoustic response generated from the same orthogonal cavity at $M_\infty = 0.3$, as shown in figure 5(a). However, contrary to previously established expectations, the inclined cavities at this Mach number produce an entirely unexpected result. First, the fundamental peak frequency is shifted to a lower value of $St \approx 0.27$. It is noteworthy that previous studies on orthogonal deep cavities by [8, 9, 24, 25] also reported a critical resonance occurring at a similar frequency, which does not conform to existing flow-acoustic resonance theories. Second, and more importantly, the inclined cavities generated a significant increase in the peak amplitude by nearly 30 dB compared to the orthogonal cavity case and by more than 10 dB even compared to the “optimal” flow-acoustic resonance at $M_\infty = 0.2$. The observed shift in the fundamental peak frequency and substantial increase in peak amplitude for the inclined cavities at $M_\infty = 0.3$ suggest novel flow-acoustic interaction mechanisms at play. Therefore, this paper aims to investigate the underlying physical processes responsible for these unexpected and profound results.

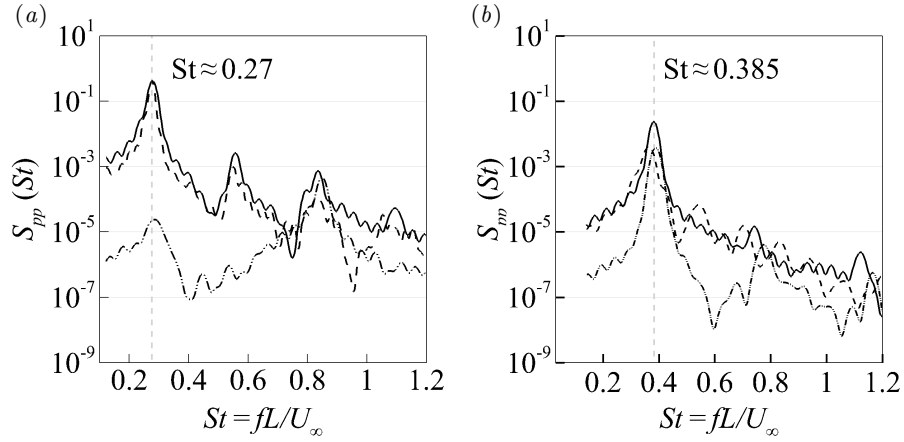


FIG. 5. Power spectral density (PSD) of the spanwise-averaged time signal of wall-pressure fluctuations measured on the base surface of the deep cavities with the inclinations: (----) $\alpha = 90^\circ$, (—) 60° , and (---) 30° at free-stream Mach numbers (a) $M_\infty = 0.3$ and (b) $M_\infty = 0.2$, respectively.

Figure 6 shows snapshots of the spanwise-averaged instantaneous pressure fluctuations captured at four sequential time intervals, each offset by $T/4$, where $T = 1/f_p$ represents the oscillation period corresponding to the tonal frequency identified in the pressure spectra of figure 5(a). These snapshots vividly capture the synchronization between shear-layer deflections and the instantaneous pressure oscillations within the deep and inclined cavities. For brevity, the subsequent analysis will primarily focus on the time variation of the instantaneous pressure fluctuations in the $\alpha = 60^\circ$ inclined cavity. Accordingly, valuable insights can be gained from the visualizations presented, focusing on the acoustic pressure averaged over the bottom surface of the inclined cavity, which is determined as

$$\chi(t) = \frac{1}{A_b} \int_{A_b} p'(\mathbf{x}_b, t) dA, \quad (18)$$

where x_b and A_b denote the Cartesian coordinates on the surface area of the cavity base, respectively.

Figure 6(a) shows the beginning of an oscillation cycle of χ , during which a distinct large-scale vortex is located slightly above the cavity opening, as revealed by the low-pressure zone near the downstream corner. At this juncture, nearly complete destructive interference occurs between the reflected compressive waves (i.e., $p' > 0$) and the incident rarefaction acoustic waves (i.e., $p' < 0$), resulting in an acoustic pressure equilibrium within the cavity (i.e., $\chi = 0$). Subsequently, the initial downward deflection of the shear-layer becomes apparent, accompanied by the emergence of low-pressure regions close to the upstream corner. The former occurrence denotes the inception of constructive interference of rarefaction acoustic waves within the cavity, while the latter event signifies the generation of vortices near the upstream corner.

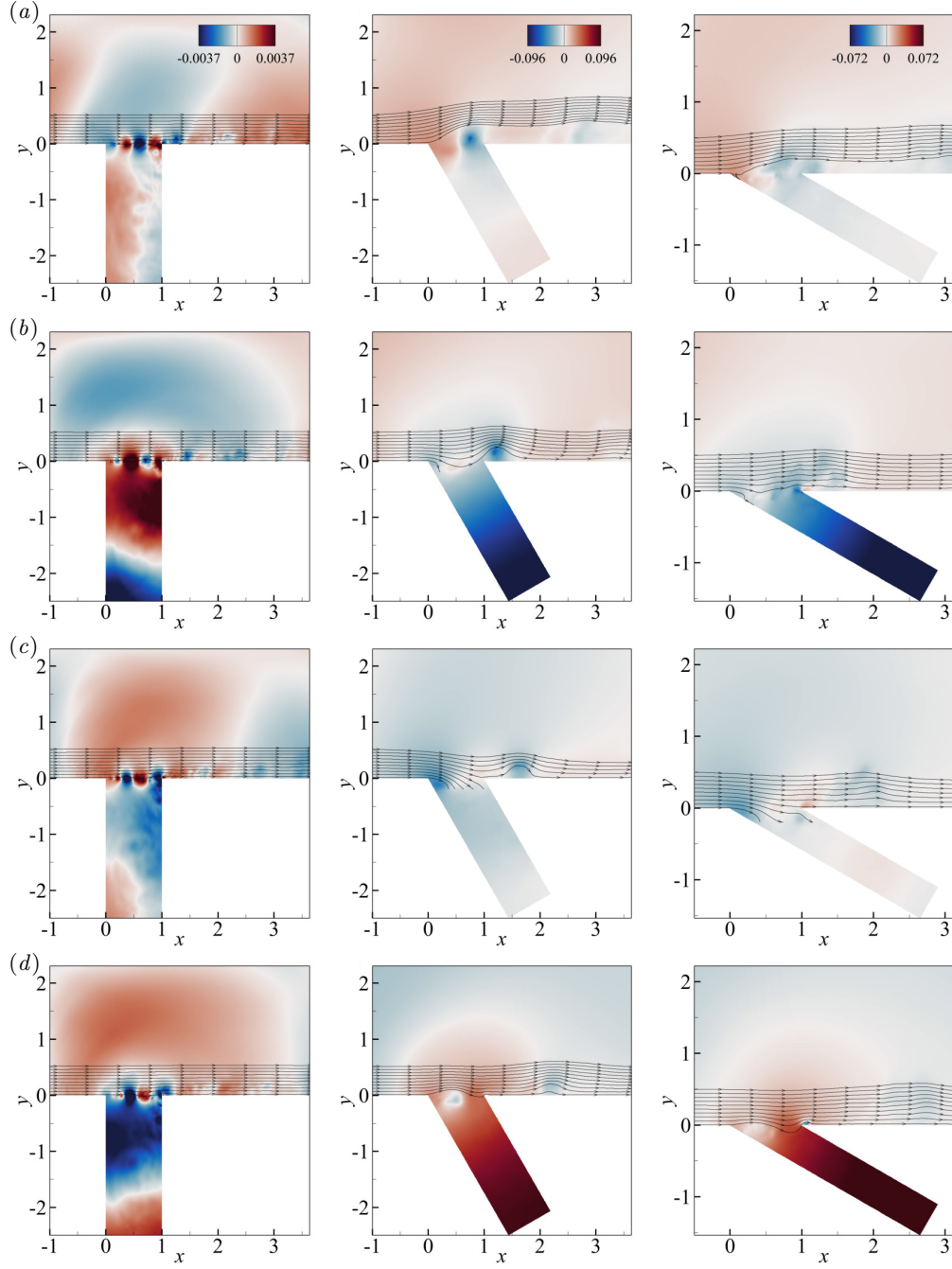


FIG. 6. Snapshots of the spanwise-averaged instantaneous pressure fluctuations, p' , with superimposed streamlines to signify the shear-layer undulation across the cavity opening with a time interval of $T/4$ between two successive plots from (a) to (d), where T is the period of the oscillation cycle of χ . The first, second, and third columns correspond to deep cavities with the inclinations $\alpha = 90^\circ$, $\alpha = 60^\circ$, and $\alpha = 30^\circ$, respectively. Here, the compressive (i.e., $p' > 0$) and rarefaction (i.e., $p' < 0$) acoustic waves are visualised by the red and blue regions in the interior of the cavity.

As the large-scale vortical structure continues its movement beyond the downstream wall, the vortex-corner interaction becomes more pronounced, generating additional rarefaction waves (i.e., $p' < 0$). These rarefaction waves interfere constructively with the waves reflected from the base of the cavity, resulting in a further reduction of the acoustic pressure fluctuations within the cavity until the acoustic pressure exerted on the cavity base reaches its minimum value, as depicted in figure 6(b). Subsequently, a distinct low-pressure region (i.e., coherent vortex) near the upstream corner, accompanied by the downward deflection in the shear-layer, is observed. Following this, a localized area of non-negative pressure gradually forms near the downstream corner. This observation is attributed to the

impeded shear-layer, which indicates the onset of stagnated flows.

As the flow field is severely retarded by the downstream corner, a highly stagnated region is established, accompanied by an increase in pressure fluctuations near the downstream corner, as shown in figure 6(c). At this instant, complete destructive interference occurs between the incident compressive acoustic waves and the rarefaction waves reflected from the base of the cavity. Subsequently, constructive interference follows within the cavity until the averaged acoustic wall-pressure χ exerted on the cavity base reaches its maximum value due to complete constructive interference of compressive acoustic waves, as depicted in figure 6(d). As the shear-layer gradually detaches from the downstream corner, the flow stagnation lessens, and complete destructive interference ensues as the large-scale vortex convects downstream and slowly ejects from the cavity. This process completes a single oscillation cycle of χ .

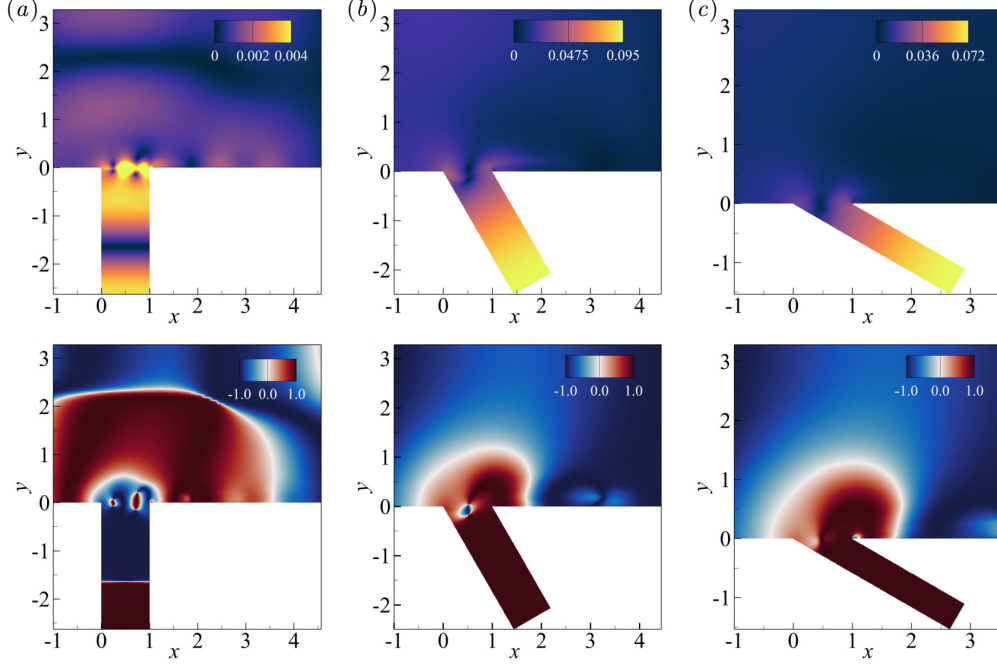


FIG. 7. The spatial distribution of the Fourier-transformed pressure fluctuations at the tonal frequency for deep cavities with the inclinations: (a) $\alpha = 90^\circ$, (b) $\alpha = 60^\circ$, (c) $\alpha = 30^\circ$, respectively. The top row of the contour plots represents the magnitude, $|p'|$, while the bottom row of the contour plots represents the cosine of the phase, $\cos(\Phi_{p'}(\mathbf{x}, f) - \Phi_\chi(\mathbf{x}, f))$. Note that $\Phi_\chi(\mathbf{x}, f)$ represents the phase of the Fourier transform of χ defined in Eq. (18).

The discussions have implicitly identified two main types of pressure fluctuations: local hydrodynamic fluctuations near the cavity opening, and acoustic fluctuations surrounding the cavity. The difference between the two components is further elucidated by the magnitude and phase distributions of the Fourier-transformed pressure fluctuations. Specifically, figure 7 reveals that the pressure field inside the cavity appears to be primarily stationary (i.e., constant phase), with a maximum magnitude (i.e., a pressure node) consistently located at the cavity base across all inclinations. This evidence suggests that the pressure field inside the cavity is predominantly acoustic in nature and contributed by the depthwise acoustic resonances. Furthermore, these resonances are highly localized within the inclined cavities and resemble the “nearly trapped acoustic mode,” that exhibits minimal radiation losses, according to Koch [16].

To facilitate subsequent investigations, we decompose the pressure fluctuations around the cavity into their hydrodynamic and acoustic components using momentum potential theory (MPT) developed by [69]. Essentially, Doak’s MPT separates the momentum density, $\rho\mathbf{u}$, into rotational and irrotational components through a Helmholtz decomposition. The Helmholtz decomposition of $\rho\mathbf{u}$ may be written as

$$\rho\mathbf{u} = \mathbf{B} - \nabla\psi, \quad \nabla \cdot \mathbf{B} = 0, \quad (19)$$

where \mathbf{B} and $\nabla\psi$ are the solenoidal and irrotational components of $\rho\mathbf{u}$, respectively. Substituting Eq. (19) into the continuity equation yields a Poisson equation for the irrotational component, with a source term dependent on density fluctuation,

$$\nabla^2\psi = \frac{\partial\rho}{\partial t}. \quad (20)$$

For a single phase continuum fluid, ψ is separated into acoustic component (irrotational and isentropic, denoted ψ_A) and entropic component (irrotational and isobaric, ψ_E) components, governed by the exact equations

$$\psi = \psi_A + \psi_E, \quad \nabla^2 \psi_A = \frac{1}{c^2} \frac{\partial \rho}{\partial t}, \quad \nabla^2 \psi_E = \frac{\partial \rho}{\partial E} \frac{\partial E}{\partial t}. \quad (21)$$

Considering the low Mach number in this study, the entropy (thermal) contribution is assumed to be relatively small compared to the acoustic contribution, and therefore ψ_E is not included in the subsequent calculation. Then, the momentum equation in terms of the hydrodynamic and acoustic components is obtained by substituting Eq. (19) into the momentum equation, expressed as

$$\frac{\partial}{\partial t}(\mathbf{B} - \nabla \psi) + \nabla \cdot \left[\frac{(\mathbf{B} - \nabla \psi)(\mathbf{B} - \nabla \psi)}{\rho} - \tau_{ij} \right] + \nabla p = 0. \quad (22)$$

By taking the divergence of Eq. (22), the Poisson equation for the hydrodynamic pressure fluctuation, p'_H

$$\nabla^2 p'_H = S_H + \tilde{S}_H, \quad (23)$$

and the Poisson equation for the acoustic pressure fluctuation, p'_A

$$\nabla^2 p'_A = S_A + \tilde{S}_A, \quad (24)$$

are derived. Accordingly, the hydrodynamic and acoustic pressure fluctuations are obtained by solving the Poisson equations in Eq. (23) and Eq. (24), respectively. The numerical implementation is described extensively in [23, 70] and the evaluations of the linear (S_H and S_A) and the non-linear source terms (\tilde{S}_H and \tilde{S}_A) are detailed in [71], which are not repeated here for brevity.

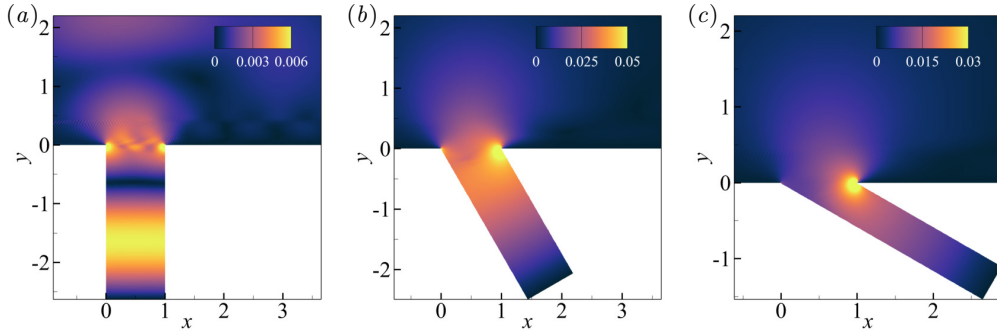


FIG. 8. The contour plots illustrate the spatial distribution of the magnitude of decomposed Fourier-transformed pressure gradient associated with the acoustic component $|\partial p_A / \partial y|(\mathbf{x}, f)$, at the tonal frequencies for deep cavities with the inclinations: (a) $\alpha = 90^\circ$, (b) $\alpha = 60^\circ$, (c) $\alpha = 30^\circ$, respectively.

Figure 8 reveals notable differences in the spatial distribution of pressure gradients for the acoustic components across orthogonal and inclined cavities. In particular, the acoustic pressure gradient tends to concentrate more intensely near the downstream corner in inclined cavities, in contrast to the symmetric distribution observed in the orthogonal cavity. This discrepancy in the spatial distribution of the acoustic pressure gradient is important for elucidating the noise generation process, which will be further discussed in Section V. Additionally, the difference in magnitude of the acoustic pressure gradient indicates that the resonant acoustic fields in inclined cavities may produce higher acoustic particle velocities compared to those in the orthogonal cavity. To quantify these observations, the induced acoustic particle velocity along the cavity opening region is approximated as being proportional to the acoustic pressure gradient, using the isentropic Euler equations [72], as expressed by

$$\frac{dv_a}{dt} = -\frac{1}{\rho} \frac{\partial p_a}{\partial y}, \quad (25)$$

where \tilde{v}_a represents the estimated acoustic particle velocity and p_a is the decomposed acoustic pressure field. Then, by considering a modal fluctuation of the acoustic pressure and spatially averaging the acoustic particle velocity across the cavity opening, we obtain an averaged acoustic particle velocity that oscillates across the cavity opening, as given by

$$\overline{v_a} = \frac{1}{L} \int_{x=0}^{x=L} \frac{1}{2\pi f} \frac{\partial p_a}{\partial y} dx. \quad (26)$$

At tonal frequencies, cavities with inclinations of ($\alpha = 90^\circ$, 60° , and 30°) exhibit an average acoustic particle velocity across the cavity opening of approximately ($|\bar{v}_a|/U_\infty \approx 9.3 \times 10^{-3}$, 2.5×10^{-1} , and 1.1×10^{-1}), respectively. For inclined cavities, these amplitude levels traditionally indicate the “high pulsation levels”, according to Bruggeman [73]. Previous studies by Peters [8] have shown that under these conditions, the resonant field can alter the vortex trajectory, forcing the vortex to enter and exit the cavity, rather than following the parallel path of the unperturbed shear-layer. The intense flow dynamics described are consistent with the temporal evolution of instantaneous pressure fluctuations and shear-layer oscillations observed in the current study, as previously shown in figure 6. In contrast, the acoustic particle velocity magnitude in the orthogonal cavity corresponds to the “low pulsation levels”, indicating the subdued shear-layer oscillation, as will be further visualized later in figure 13.

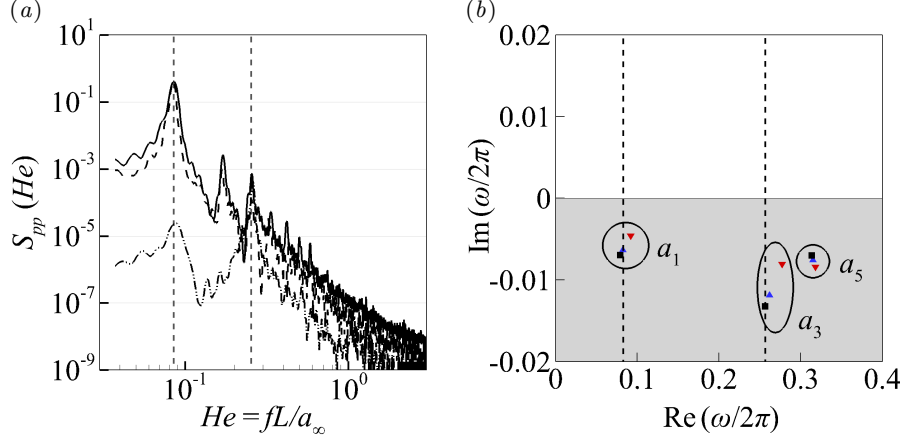


FIG. 9. (a) Power spectral density (PSD) of the spanwise-averaged wall-pressure fluctuations at $M_\infty = 0.3$, with frequency expressed as Helmholtz number (He), compared with (b) the first three least-damped acoustic modes or eigenmodes obtained from the modal analysis of APEs for cavities with inclinations of (■) $\alpha = 90^\circ$, (▲) 60° , and (▼) 30° , respectively. Vertical dashed lines (---) indicate the tonal frequencies observed in the current cavity configurations, see pressure spectra in figure 5.

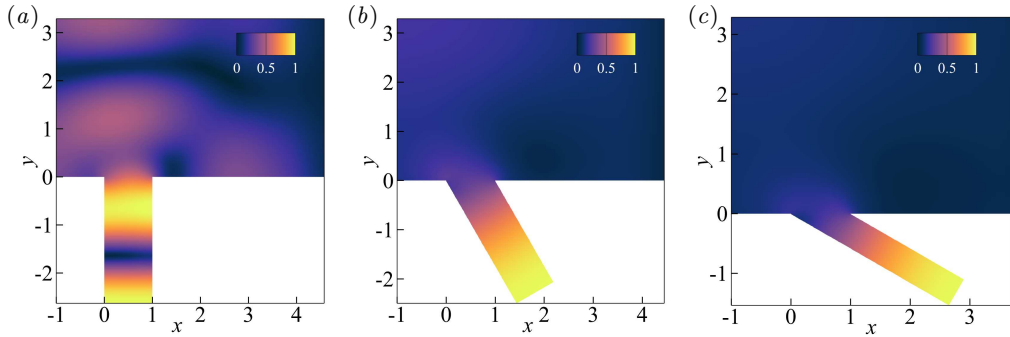


FIG. 10. The contour plots show the spatial distribution of the pressure magnitude of the eigenmode nearest to the tonal frequency, for cavities with inclinations of (a) $\alpha = 90^\circ$, (b) $\alpha = 60^\circ$, and (c) $\alpha = 30^\circ$, respectively. For fair comparisons, the magnitude of the eigenvector is normalised such that it is unity at the base of the cavity.

Figure 9(a) presents a comparison of pressure spectra for all cavity oscillations at $M_\infty = 0.3$, similar to that shown in figure 5(a), with frequencies here expressed in Helmholtz numbers, $He = fL/a_\infty$, to enable direct comparison with the first three least-damped acoustic modes (eigenmodes) obtained from the modal analysis of APEs. These acoustic eigenmodes are characterized by complex resonance frequencies, with the real part indicating the physical resonance frequencies and the imaginary part measuring the radiation losses (i.e., damping) of the resonances, as outlined in Subsection IID. Figure 9(b) shows that the tonal frequencies of the cavity oscillations at $M_\infty = 0.3$ all reside close to their respective acoustic eigenmodes, highlighting the crucial role of acoustic resonances in selecting the oscillation frequency in deep and inclined cavities. Specifically, the comparison reveals that the orthogonal cavity oscillation is predominantly excited by the third depthwise acoustic mode, a_3 , which has higher radiation losses. In contrast, inclined cavity oscillations are excited by the first depthwise acoustic mode, a_1 , which exhibits considerably lower radiation losses. This disparity in radiation losses could provide a quantitative explanation for the differences

in acoustic particle velocity fields observed between orthogonal and inclined cavities. As Koch [16] suggests, acoustic modes with higher radiation losses (i.e., a greater negative imaginary part of the complex frequency) tend to radiate and dissipate more energy into the surroundings. Consequently, the higher radiation losses of the third mode in the orthogonal cavity lead to a wider distribution of acoustic energy compared to the more localized distribution of the first mode in inclined cavities, as visualized in figure 10.

IV. HYDRODYNAMIC FIELDS

In this section, we discuss the hydrodynamic fields near the cavity opening in detail. As mentioned, the location of the coherent vortical structure is crucial to the acoustic emission process. Therefore, an accurate description of the position and path traveled by the vortical structure, which is a function of time, is essential for this investigation. Generally, the location of the vortical structure can be approximated using the pressure minima technique, as shown in Section III. However, it is challenging to justify an accurate quantification of the hydrodynamic mode based on the number of discrete low-pressure spots [23]. To overcome this limitation, the location of the vortical structure is identified using the equivalent Q -criterion [74], which is given by

$$Q = \epsilon_{ij}\epsilon_{ji} - \frac{1}{2}\omega_i^2 \approx -\nabla^2 \tilde{p}_H / \rho_\infty, \quad (27)$$

where $\epsilon_{ij} = \frac{1}{2}(\partial u_i / \partial x_j + \partial u_j / \partial x_i)$ represents the rate of strain, ω_i denotes the vorticity of the velocity field, and $\nabla^2 \tilde{p}_H$ is the Laplacian of the hydrodynamic pressure field. This formulation offers two distinct advantages: first, Eq. (27) establishes a direct link between the velocity gradient field and the hydrodynamic pressure field to accurately pinpoint the location of the vortex. Second, the positive and negative values of the Q -criterion provide valuable insights into the strain rate and vorticity of the velocity fields, which are essential for understanding subsequent noise generation mechanisms [75].

Figure 11 shows an oscillation cycle of χ similar to that of figure 6, with particular attention now given to the vortex dynamics near the cavity opening region. The Q -criterion, calculated from Eq. (27), is plotted and superimposed with streamlines to indicate the shear-layer oscillations near the cavity opening. We will examine the vortex dynamics within the $\alpha = 60^\circ$ inclined cavity. Figure 11(a) shows the instant when a large-scale vortex, characterized by $Q < 0$, is located slightly above the cavity opening line at the downstream corner. The vorticity-dominated region near the downstream walls is associated with low hydrodynamic pressure ($p'_H < 0$) and is visualized in figure 12. These hydrodynamic wall-pressure fluctuations act as a dipole noise source from the surface integral of Curle's equation [76], which were previously identified as the dominant noise source in both shallow and deep cavities [77, 78]. Therefore, the presence of low hydrodynamic wall-pressure fluctuations ($p'_H < 0$) correspond to generating rarefaction acoustic waves ($p'_A < 0$), which at this point destructively interfere with compressive acoustic waves ($p'_A > 0$) reflected from the cavity base during the preceding cycle. This destructive interference leads to the acoustic pressure equilibrium within the cavity (i.e., $\chi = 0$), as previously shown in figure 6(a).

As the large-scale vortex sweeps past the downstream corner, it induces stronger interaction with the vorticity field and the downstream walls. At this stage, the additional rarefaction waves undergo constructive interference with the acoustic waves reflected from the base of the cavity, until the large-scale vortex is completely ejected from the cavity, as shown in figure 11(b). The ejection of the vortex triggers an immediate downward deflection of the shear-layer near the upstream corner, accompanied by the emergence of small-scale vortices within the separated shear-layer. These small vortices gradually grow and merge, eventually forming a single large-scale vortex near the upstream corner, as illustrated in figure 11(c). The further downstream convection and development of this large-scale vortex before completing the feedback oscillation cycle is shown in figure 11(d). In contrast to the orthogonal cavity case, the recurring interaction between the escaping vortical structure and the downstream corner in inclined cavities mirrors the well-documented phenomenon of “vortex above corner” interaction, as reported by Tang and Rockwell [79].

Additionally, we employ the Direct Lyapunov Exponents (DLE) method introduced by Haller [80, 81] to identify the Lagrangian Coherent Structures (LCS) present in the turbulent cavity flow fields. The DLE field is defined as

$$\text{DLE}_{\Delta T}(x_0, t_0) = \frac{1}{2\Delta T} \log(\sigma_T(x_0, t_0)), \quad (28)$$

where σ_T represents the square of the largest singular value of the deformation gradient $\partial x(t_0 + \Delta T, x_0, t_0) / \partial x_0$ such that

$$\sigma_T(x_0, t_0) = \lambda_{\max} \left(\left[\frac{\partial x(t_0 + \Delta T, x_0, t_0)}{\partial x_0} \right]^T \left[\frac{\partial x(t_0 + \Delta T, x_0, t_0)}{\partial x_0} \right] \right), \quad (29)$$

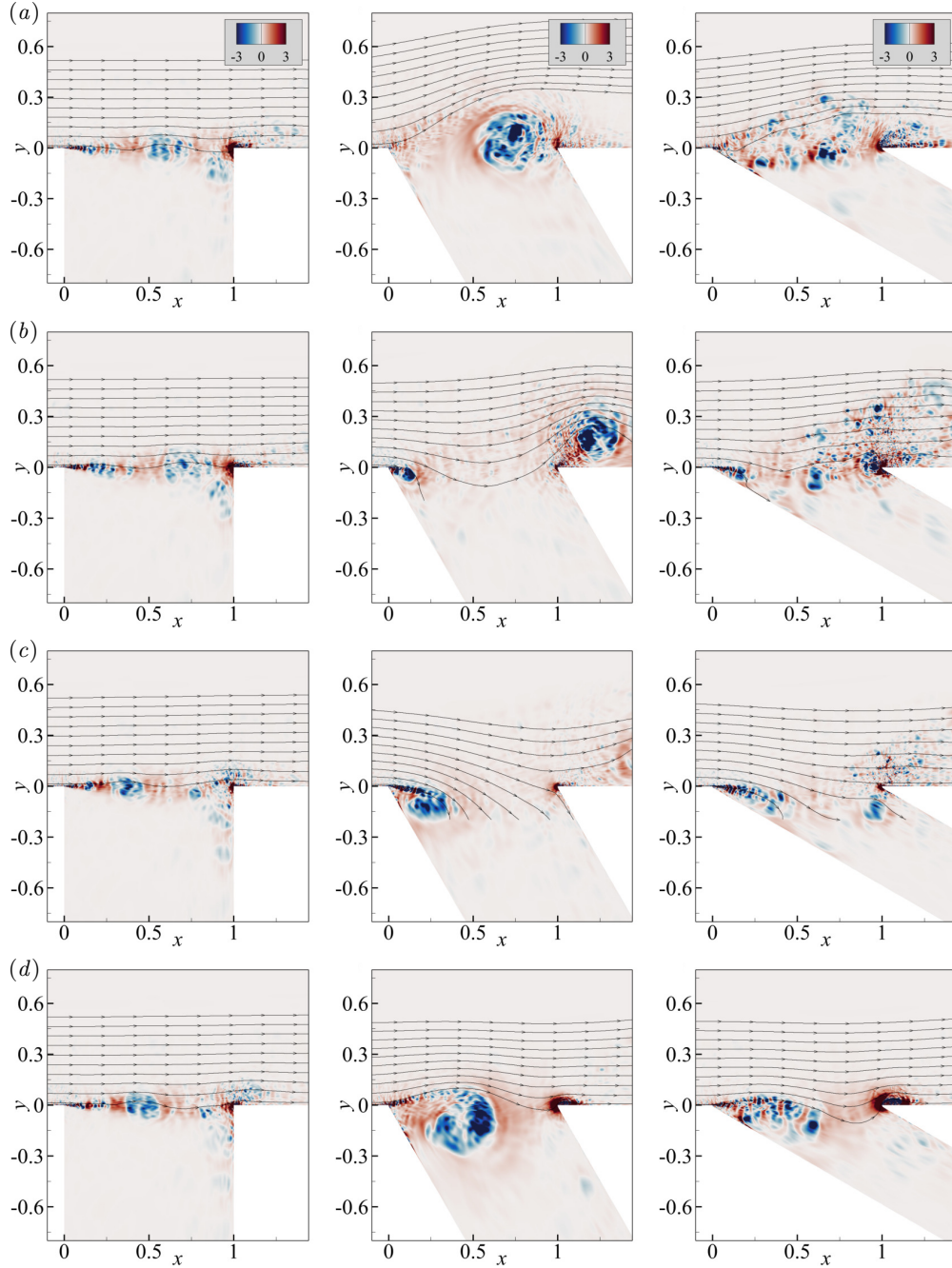


FIG. 11. Snapshots of the spanwise-averaged instantaneous Q -criterion with superimposed streamlines to signify the shear-layer undulation across the cavity opening with a time interval of $T/4$ between two successive plots from (a) to (d), where T is the period of the oscillation cycle of χ . The first, second, and third columns correspond to deep cavities with the inclinations: $\alpha = 90^\circ$, $\alpha = 60^\circ$, and $\alpha = 30^\circ$, respectively. For the corresponding hydrodynamic pressure fields, see Figure 12.

and $x(t, x_0, t_0)$ denotes the position of a particle at time t , initiating at position x_0 at time t_0 . In this paper, the DLE field is calculated by integrating trajectories in backward time ($\Delta T < 0$) and the ridges in the DLE field capture attracting Lagrangian coherent structures (attracting LCS) in the flow field [80]. The integration time, ΔT , is adjusted to achieve the desired level of detail in the calculation without compromising the location of the attracting LCS boundary. Figure 13 shows that the DLE field clearly depicts the vortices within the subdued and nearly parallel shear-layer oscillations observed in the orthogonal cavity, as well as the intense shear-layer roll-up and subsequent coherent structure formation in the inclined cavities.

From these flow visualizations, it is apparent that the intense shear-layer deflections and the non-parallel trajectory

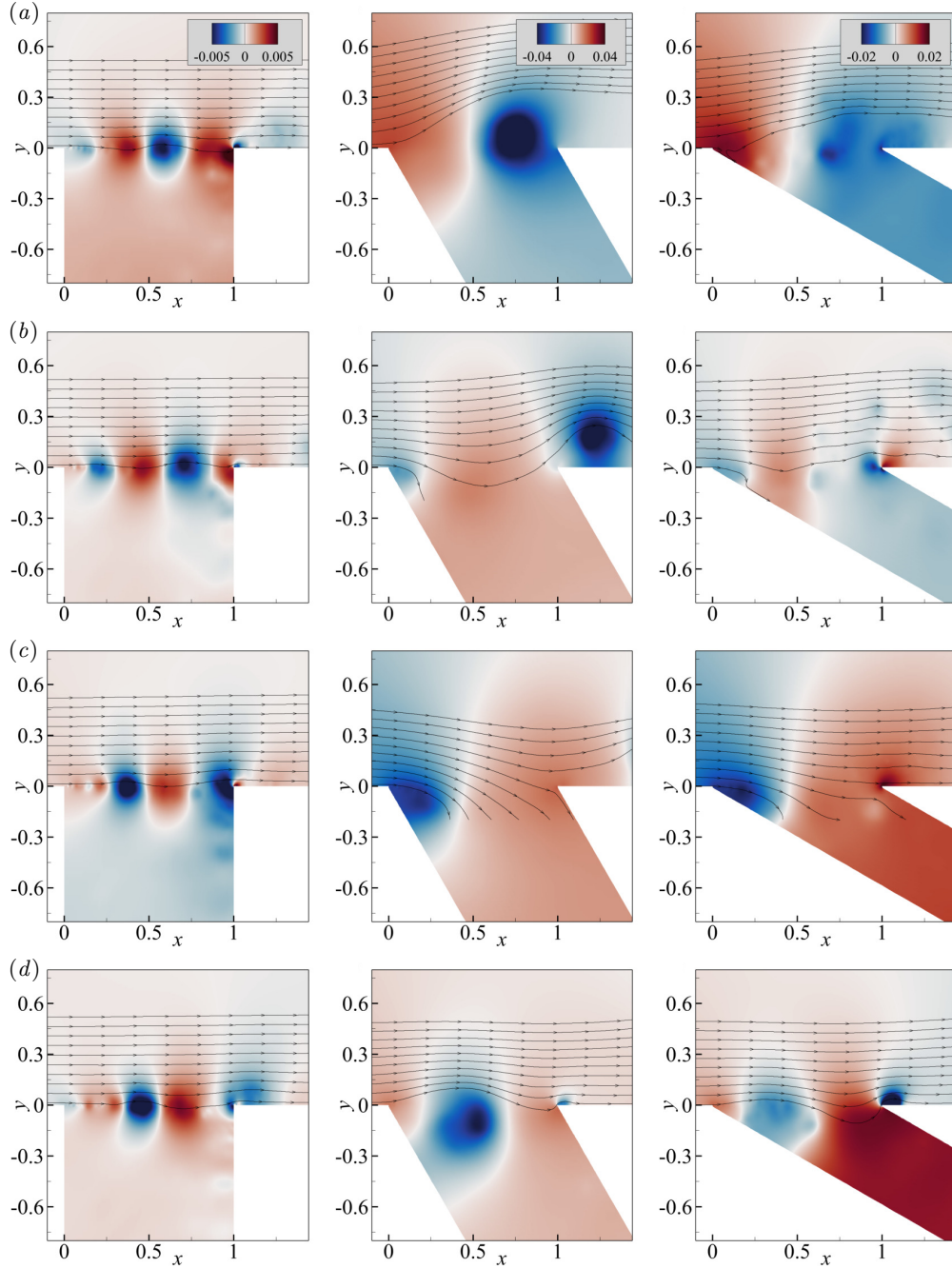


FIG. 12. Snapshots of the spanwise-averaged instantaneous hydrodynamic pressure fluctuation p'_H with superimposed streamlines to signify the shear-layer undulation across the cavity opening with a time interval of $T/4$ between two successive plots from (a) to (d), where T is the period of the oscillation cycle of χ . The first, second, and third columns correspond to deep cavities with the inclinations $\alpha = 90^\circ$, $\alpha = 60^\circ$, and $\alpha = 30^\circ$, respectively.

of the large-scale vortex within the $\alpha = 60^\circ$ inclined cavity closely resemble the phenomena observed in closed side-branches [82]. This similarity suggests that the deflection of the shear-layer may primarily result from the vertical forcing generated by the time-varying mass flow rate traversing the cavity opening. To further investigate this phenomenon, the total mass forcing through the cavity opening, denoted as $d\dot{m}/dt$, is decomposed into solenoidal and irrotational components by performing an integration of the rate of change of vertical momentum-density across the

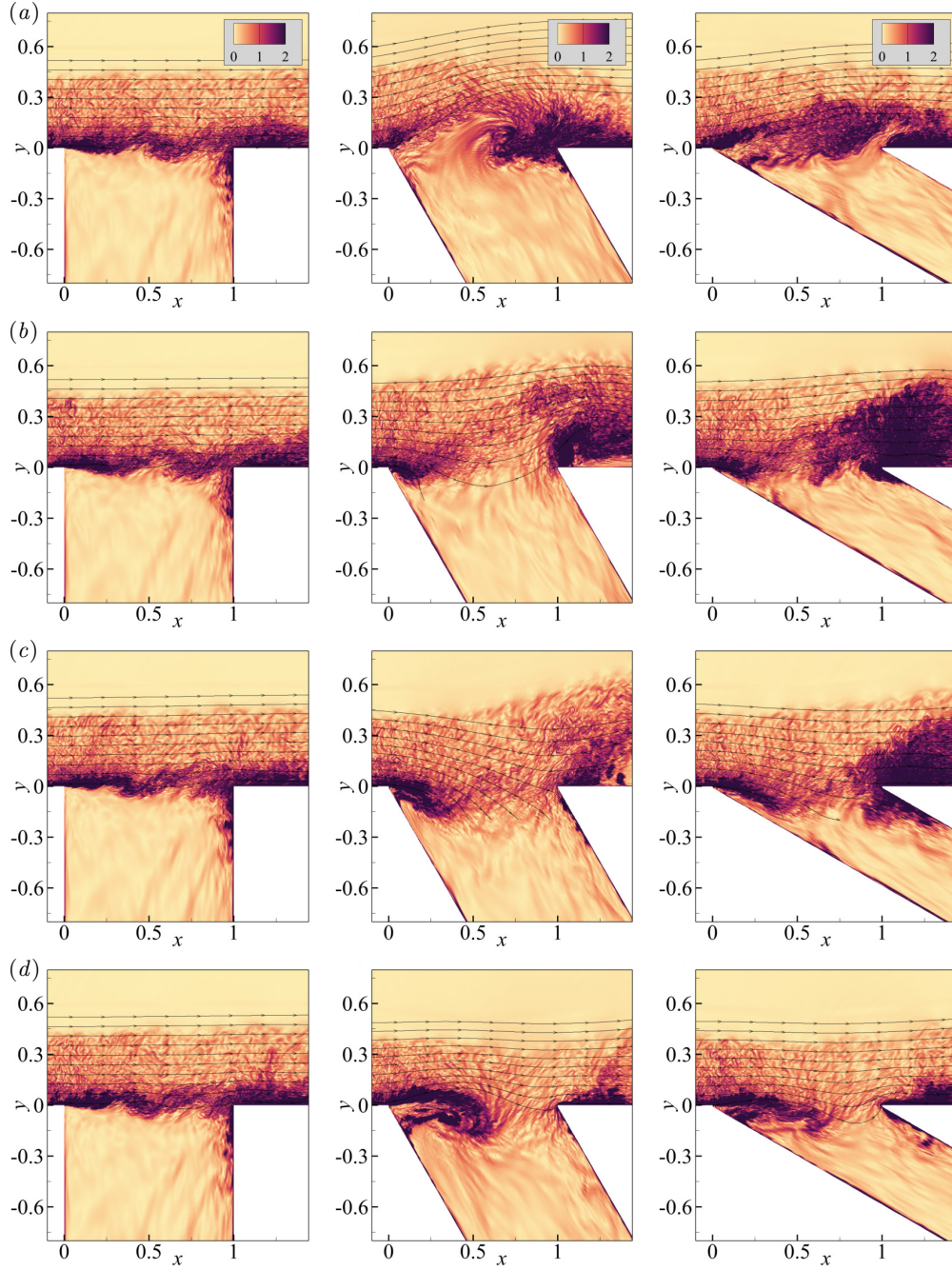


FIG. 13. Snapshots of the spanwise-averaged instantaneous DLE with superimposed streamlines to signify the shear-layer undulation across the cavity opening with a time interval of $T/4$ between two successive plots from (a) to (d), where T is the period of the oscillation cycle of χ . The first, second, and third columns correspond to deep cavities with the inclinations $\alpha = 90^\circ$, $\alpha = 60^\circ$, and $\alpha = 30^\circ$, respectively. For the corresponding Q -criterion fields, see Figure 11.

cavity opening in the streamwise direction, such as

$$\frac{dm_A}{dt}(t) = -\frac{1}{dt} \int_0^L \nabla \psi_A(x, y=0, t) dx, \quad (30a)$$

$$\frac{dm_H}{dt}(t) = \frac{1}{dt} \int_0^L B_y(x, y=0, t) dx. \quad (30b)$$

Furthermore, the shear-layer deflections near the upstream corner are quantified by monitoring the vertical coordinate

of the streamtrace near the location at $x = -0.2$. Figure 14(*a,b*) shows the space-time contour plots of the rate of change of decomposed vertical momentum density across the cavity opening (i.e., $y = 0$), where the solenoidal component B_y induced by the large-scale vortex is highly localized in space compared to the uniformly distributed irrotational component $\nabla\psi_A$. From Figure 14(*c*), it is apparent that shear-layer deflections near the upstream corner are closely synchronized with the rate of change of the acoustical mass flow rate induced by the depthwise acoustic resonance, thereby highlighting the dominant influence of the spatially coherent depthwise acoustic resonance on the observed intense shear-layer oscillations.

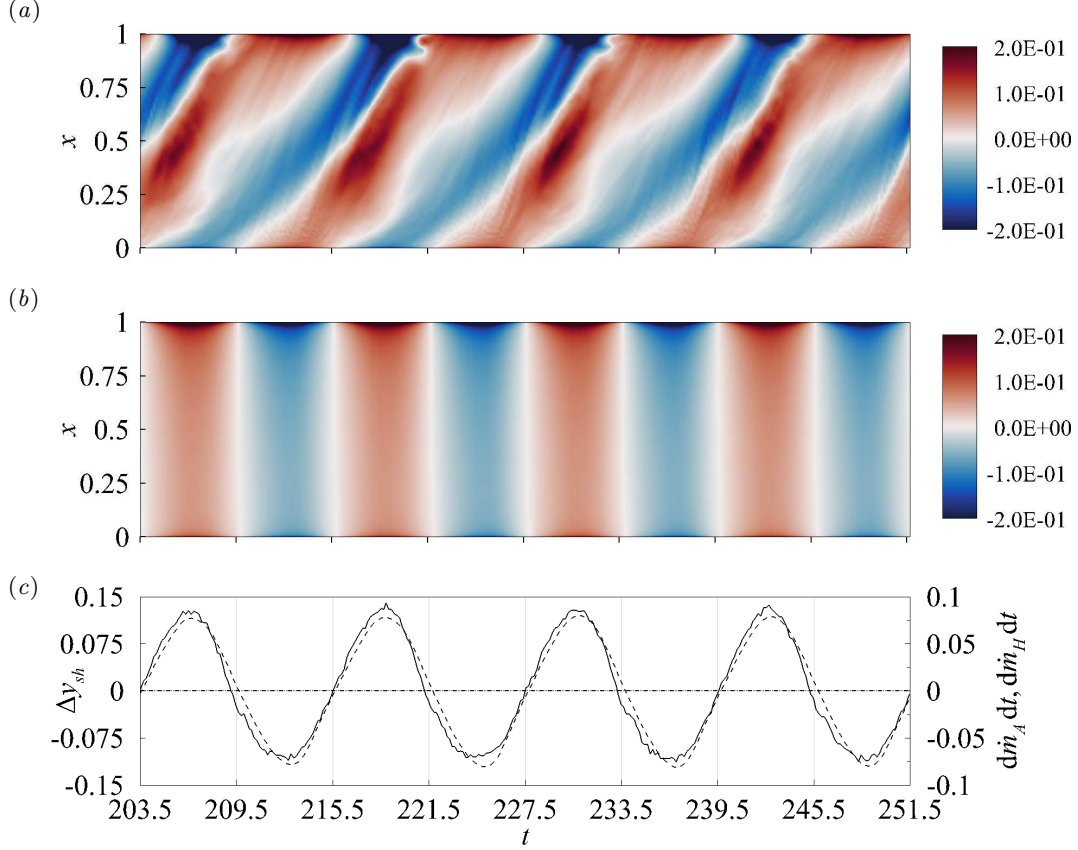


FIG. 14. The space-time contour plots of (*a*) the solenoidal (hydrodynamic) component; (*b*) the irrotational (acoustic) component of the rate of change of vertical momentum-density, $\partial(\rho v)/\partial t$, across the cavity opening in the downstream direction at $y = 0$; and (*c*) the time variation of integrated vertical momentum-density rates for (---) the acoustic component as calculated from Eq. 30(*a*), (-·-) the hydrodynamic component as calculated from Eq. 30(*b*); and the vertical coordinate of the shear-layer oscillation measured near the upstream corner at $x = -0.2$ (—) for the $\alpha = 60^\circ$ inclined cavity case.

Additionally, the streamwise phase variation of the Q -criterion across the cavity opening in orthogonal and inclined cavities is shown in figure 15. This corresponds to the second (i.e., $n = 2$) and first (i.e., $n = 1$) hydrodynamic modes that satisfy the correct phase criterion of $\Delta\Phi_Q(\mathbf{x}, f_p) = 2\pi n$, according to Rockwell and Naudascher [83]. However, significant differences in the average convection speed of these hydrodynamic modes are observed between the orthogonal and inclined cavity cases, as shown in table II. To explain these discrepancies, the trajectories of the coherent vortices are tracked through the Fourier-transformed magnitude of the Q -criterion, and the time-averaged streamwise velocities along their respective paths are recorded, as shown in figure 16. The results reveal that the second hydrodynamic mode (i.e., coherent vortices) in the orthogonal cavity traverses the cavity opening at a faster convection speed (i.e., $K_c = 0.424$) due to its nearly parallel trajectory relative to the faster mean flow. In contrast, the first hydrodynamic mode (i.e., large-scale vortex) in inclined cavities convects at a slower speed (i.e., $K_c = 0.276$). This slower convection is attributed to the downward trajectory of the vortex into the cavity interior where the mean flow is slower, resulting in a longer travel time per cycle and self-sustained oscillations at a lower frequency of $St \approx 0.27$ compared to the orthogonal cavity case.

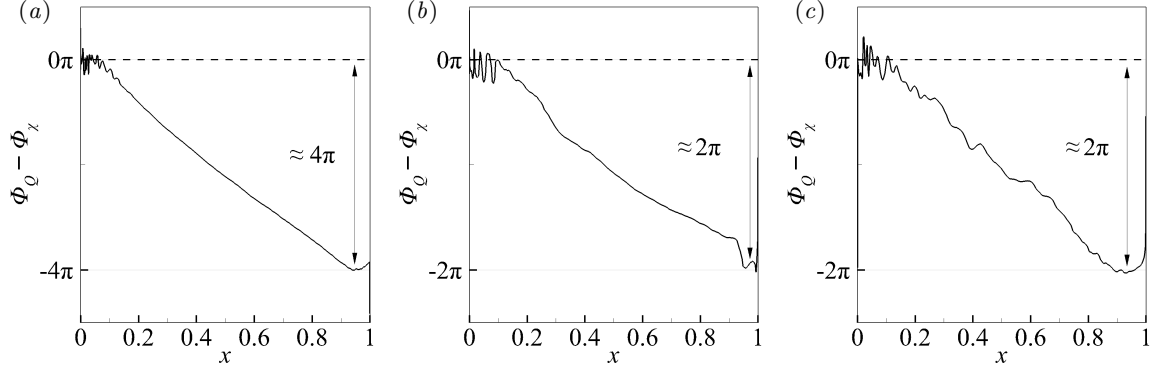


FIG. 15. The streamwise phase variation of the Fourier-transformed Q -criterion, $\Phi_Q(\mathbf{x}, f)$, measured across the cavity opening (i.e., at $y = 0$) at their respective tonal frequencies for cavities with inclinations of (a) $\alpha = 90^\circ$, (b) $\alpha = 60^\circ$, and (c) $\alpha = 30^\circ$, respectively. Note that the spatial variation of $\Phi_Q(\mathbf{x}, f)$ is calculated based on the phase reference of $\Phi_\chi(\mathbf{x}, f)$.

α	fL/a_∞	$\Delta\Phi_{V_H}/2\pi$	$M_c = U_c/a_\infty$	$K_c = U_c/U_\infty$
30°	0.0828	≈ 1.00	0.0828	0.276
60°	0.0828	≈ 1.00	0.0828	0.276
90°	0.2548	≈ 2.00	0.1274	0.424

TABLE II. The average convection speed ratio, $K_c = U_c/U_\infty$, of the vortical structures at each tonal frequency is calculated based on the streamwise phase variation of the Fourier-transformed Q -criterion, $\Phi_Q(\mathbf{x}, f)$, measured across the cavity opening (i.e., $y = 0$) using the linear dispersion relation, considering the free-stream Mach number of $M_\infty = 0.3$ for cavities with inclinations of $\alpha = 90^\circ$, $\alpha = 60^\circ$, and $\alpha = 30^\circ$, respectively.

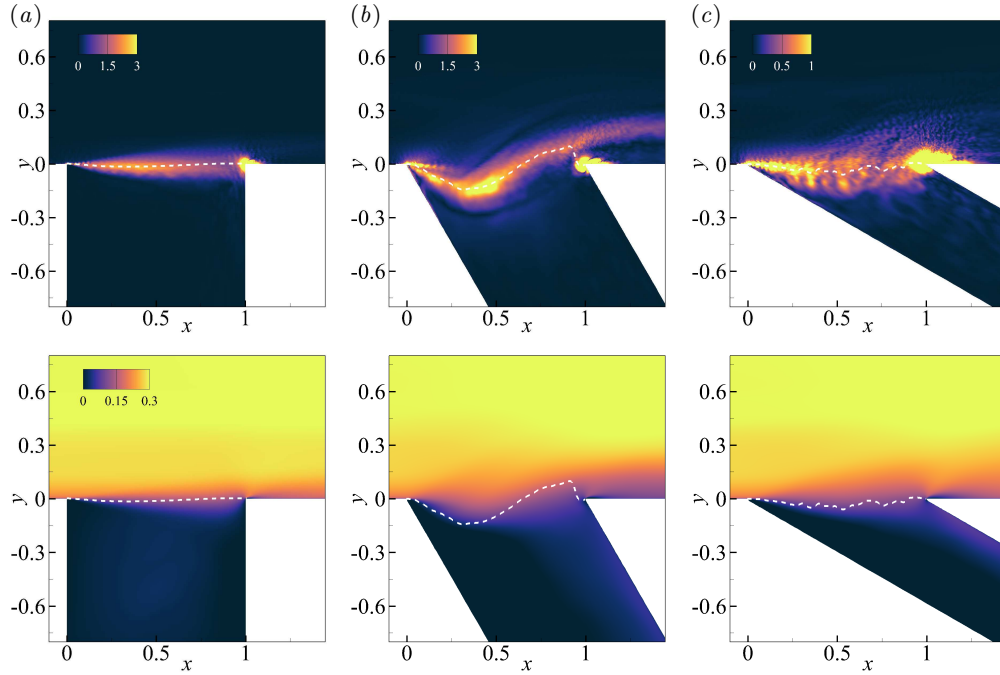


FIG. 16. The top row of contour plots presents the spatial distribution of the Fourier-transformed magnitude of the Q -criterion, $|Q(\mathbf{x}, f)|$, while the bottom row of contour plots shows the spatial distribution of the time-averaged streamwise velocity. The cavities with the inclinations are shown in (a) $\alpha = 90^\circ$, (b) $\alpha = 60^\circ$, and (c) $\alpha = 30^\circ$, respectively. The (---) trajectory of the vortical structures is traced by monitoring the maximum value of $|Q(\mathbf{x}, f)|$ near the cavity opening, and this tracked trajectory is superimposed onto the time-averaged streamwise velocity contour plot for visual comparison.

V. AEROACOUSTIC MODE AMPLIFICATIONS AND SELECTIONS

Section IV has highlighted that the depthwise acoustic resonance in inclined cavities plays a crucial role in controlling and synchronizing the deflection of the shear-layer near the upstream corner. This important physical phenomenon not only facilitates the generation of vorticity but also results in dominant noise sources when coupled with resonant acoustic fields. The mechanisms of sound generation by vortex shedding in resonant acoustic fields were established in Vortex Sound Theory [84, 85]. An essential aspect of this theory is the quantification of the instantaneous acoustic source power, Π , which can be estimated using the following approximation

$$\Pi \approx -\rho_\infty \iint_{\mathbf{x}} (\boldsymbol{\omega} \times \mathbf{u}) \cdot \mathbf{u}_a d\mathbf{x}, \quad (31)$$

where $\boldsymbol{\omega}$ is the vorticity vector and \mathbf{u}_a refers to the acoustic particle velocity vector. The triple-dot product $((\boldsymbol{\omega} \times \mathbf{u}) \cdot \mathbf{u}_a)$ provides quantitative insight into the local energy transfer between the hydrodynamic and acoustic fields. In particular, the integrand captures the transfer of acoustic energy to hydrodynamic energy (e.g., $(\boldsymbol{\omega} \times \mathbf{u}) \cdot \mathbf{u}_a > 0$) and vice versa. For sustained oscillations to occur, it is crucial for the integral in Eq. (31) to remain positive over an acoustic cycle, implying that a favorable phase relationship between the Lamb vector $(\boldsymbol{\omega} \times \mathbf{u})$ and the acoustic field, \mathbf{u}_a , must be maintained throughout the cycle. To further discuss this energy exchange process, the ensuing discussion will explore the temporal dynamics of the Lamb vector within resonant acoustic fields in inclined cavities.

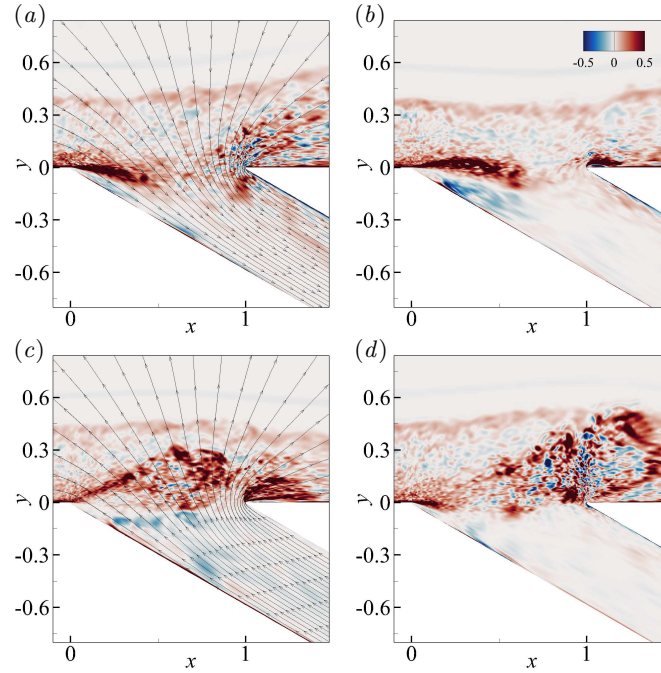


FIG. 17. The time evolution of the Lamb vector $(\boldsymbol{\omega} \times \mathbf{u})$ in the vertical direction for the $\alpha = 30^\circ$ inclined cavity is examined for a single acoustic cycle. The contour plots capture two key time instants: those (a) when the instantaneous acoustic source power, Π , reaches its minimum, and (c) when it reaches its maximum. The contour plots (b,d) indicate the time junctures when the instantaneous acoustic source power becomes zero, such as when $\Pi = 0$. Here, the superimposed streamline represents the instantaneous acoustic particle velocity field.

Figure 17 shows the time evolution of the Lamb vector and the acoustic particle velocity field in an $\alpha = 30^\circ$ inclined cavity over an acoustic cycle. The acoustic absorption phase is depicted in figures 17(a,b), where hydrodynamic instabilities within the shear-layer absorb acoustic energy to form a coherent vortex near the upstream corner, while the residual vorticity near the downstream corner from the preceding cycle also contributes to this absorption. The second half of the acoustic production phase is captured in figures 17(c,d), where the vorticity-dominated regions are now in phase with the acoustic particle velocity field until their ejection from the cavity in the same direction as the acoustic particle velocity. Subsequently, figure 18 shows the time evolution of the Lamb vector and the acoustic particle velocity field in the $\alpha = 60^\circ$ inclined cavity over an similar acoustic cycle. Although there are significant similarities with the $\alpha = 30^\circ$ inclined cavity, two key differences are observed. First, the vortex structure in the $\alpha = 60^\circ$ inclined cavity exhibits enhanced spanwise coherence, contributing to a more pronounced Lamb vector

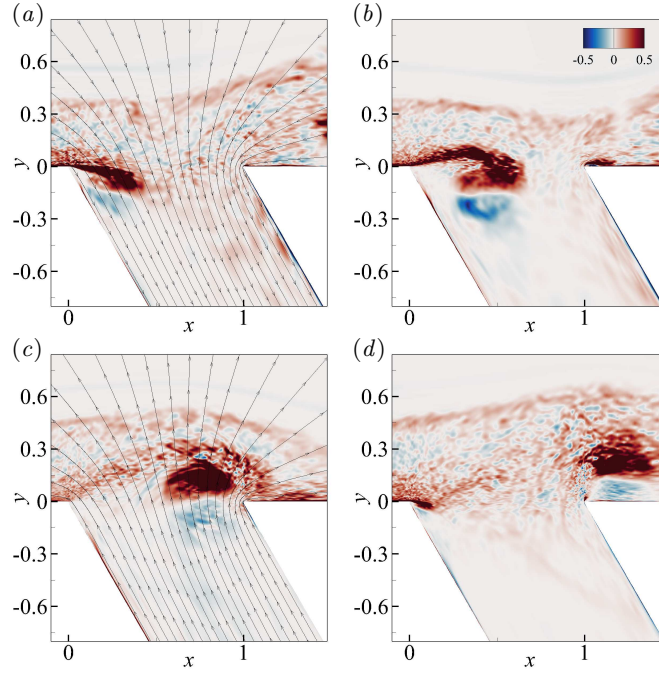


FIG. 18. The time evolution of the Lamb vector ($\omega \times \mathbf{u}$) in the vertical direction for the $\alpha = 60^\circ$ inclined cavity is examined for a single acoustic cycle. The contour plots capture two key time instants: those (a) when the instantaneous acoustic source power, Π , reaches its minimum, and (c) when it reaches its maximum. The contour plots (b,d) indicate the time junctures when the instantaneous acoustic source power becomes zero, such as when $\Pi = 0$. Here, the superimposed streamline represents the instantaneous acoustic particle velocity field.

and consequently enhanced instantaneous acoustic source power. Second, the diminished residual vorticity near the downstream corner in the $\alpha = 60^\circ$ inclined cavity reduces the overall absorption of acoustic energy. These factors may potentially explain the stronger acoustic response observed in the $\alpha = 60^\circ$ inclined cavity.

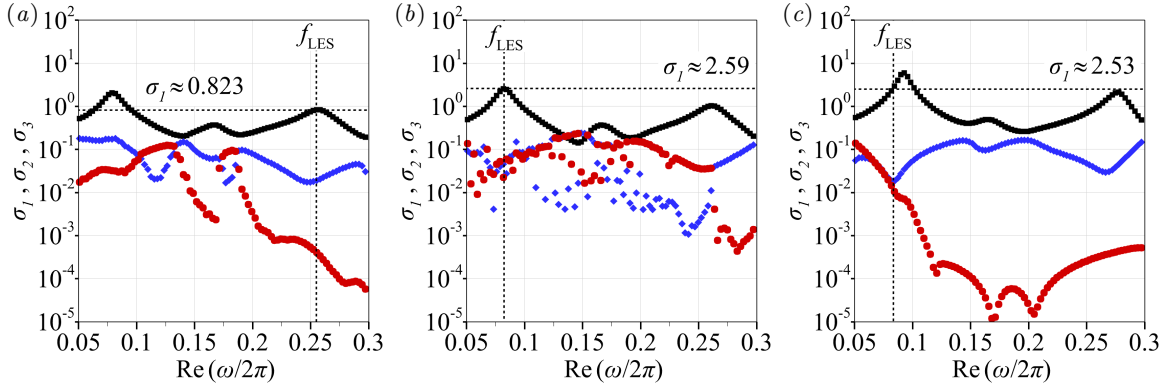


FIG. 19. The low-rank behavior of the acoustic input-output operator is visualized through the first three leading magnification rates; (■) σ_1 , (▲) σ_2 , and (●) σ_3 for cavities with inclinations of (a) $\alpha = 90^\circ$, (b) $\alpha = 60^\circ$, and (c) $\alpha = 30^\circ$, respectively. The vertical dashed line (---) indicates the tonal frequency observed in the LES, while the horizontal dashed line (---) represents the leading amplification rate σ_1 corresponding to that frequency.

The preceding discussion provides sufficient qualitative explanations for the intense acoustic response observed in the inclined cavities. To delve further into the intrinsic mechanism of noise amplification within these cavity flow systems, an acoustic input-output analysis, as outlined in Subsection IID, has been performed. The primary aim of this analysis is to establish a direct quantitative link between the Lamb vector and the magnitude of the acoustic response through the corresponding amplification rates and the forcing-response mode shapes of the acoustic input-output operator. Accordingly, figure 19 showcases the three leading amplification rates of the acoustic input-output operator across varying frequencies. The results indicate that the leading amplification rate significantly exceeds

the second and third rates at tonal frequencies across all cavity inclinations, highlighting the low-rank behavior of the cavity oscillations considered in this study. Thus, this low-rank behavior justifies a rank-1 approximation of the input-output operator of APEs, where the first rank sufficiently describes the acoustic response of the cavity system, such as

$$\mathbf{R}_{\bar{q},\omega} = \mathbf{U}\Sigma\mathbf{V}^* = \sum \sigma_i \mathbf{u}_i \mathbf{v}_i \approx \sigma_1 \mathbf{u}_1 \mathbf{v}_1. \quad (32)$$

In this formulation, \mathbf{u}_1 and \mathbf{v}_1 represent the leading forcing and response modes respectively, while σ_1 denotes the gain of the leading forcing-response pair. This approximation establishes a quantitative connection between the input forcing, $\hat{\mathbf{f}}_\omega$ (e.g., the Lamb vector), and the corresponding output acoustic field quantities, $\hat{\mathbf{q}}_\omega$ (e.g., the acoustic pressure fluctuations), which can be represented as

$$\hat{\mathbf{q}}_\omega = \mathbf{R}_{\bar{q},\omega} \hat{\mathbf{f}}_\omega \approx \sigma_1 \mathbf{u}_1 \mathbf{v}_1 \cdot \hat{\mathbf{f}}_\omega = \sigma_1 \mathbf{u}_1 F_\omega. \quad (33)$$

Figure 20 presents the spatial distribution of the reconstructed acoustic pressure field, which exhibits strong agreement with the LES data, thereby indicating the suitability of the rank-1 approximation for capturing the dominant acoustic characteristics of deep cavity flows examined in this study.

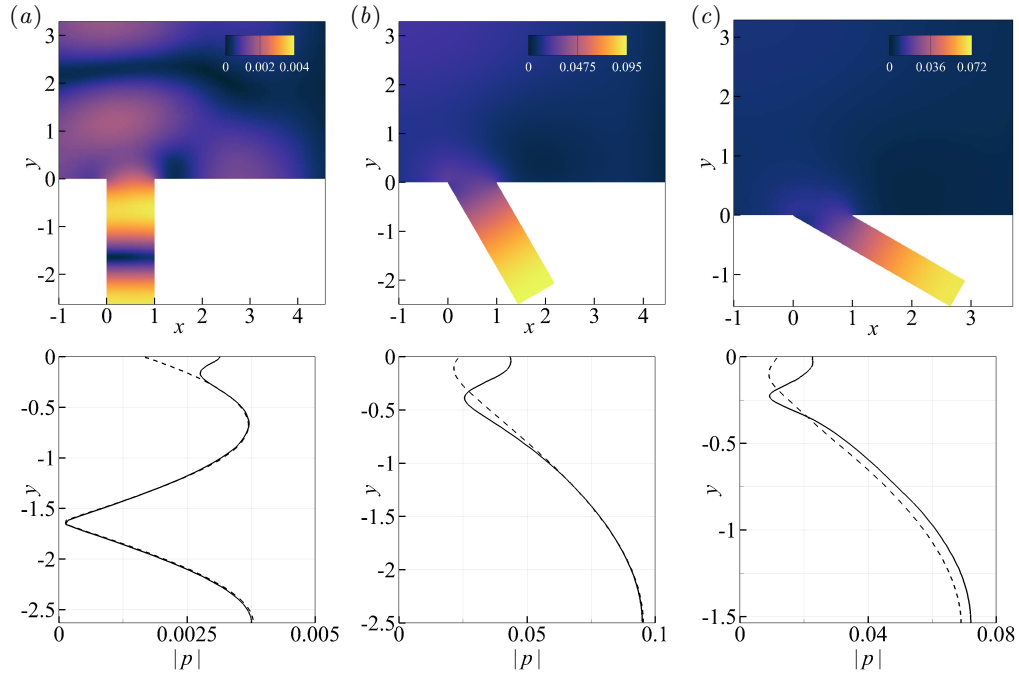


FIG. 20. The first row of contour plots shows the spatial distribution of the magnitude of the reconstructed acoustic pressure field for cavities with inclinations of (a) $\alpha = 90^\circ$, (b) $\alpha = 60^\circ$, and (c) $\alpha = 30^\circ$, respectively. The second row of line plots highlights that the depthwise distribution of wall-pressure fluctuations measured along the upstream cavity wall (i.e., $x = 0$) from the (—) LES, compare favorably with the (---) rank-1 approximation computed using Eq. (33).

Figure 21(a,b) shows the integrated-volume forcing, denoted as F_ω , and the leading gain, σ_1 , of the acoustic input-output operator. Comparing these quantities reveals several insights into the factors influencing the observed acoustic responses at different inclinations. Specifically, the weaker acoustic response in the orthogonal cavity can be attributed to two primary factors: reduced leading gain and decreased integrated-volume forcing. First, the reduced leading gain in the orthogonal cavity is caused by the excitation of the third depthwise acoustic mode, characterized by substantial radiation losses as previously shown in figure 9(b), thereby reducing the acoustic amplification. Second, the decreased integrated-volume forcing observed in the orthogonal cavity results from pronounced source-sink cancellation by the second hydrodynamic mode. This hydrodynamic mode comprises multiple vortices that exhibit destructive interferences between the source and sink regions, as visualized in figure 22(a). Consequently, it becomes evident that self-sustained oscillations with higher hydrodynamic modes (e.g., $St > 0.8$), featuring more and smaller vortices, may lead to weaker acoustic responses due to increased source-sink cancellations.

In contrast, inclined cavities exhibit stronger acoustic responses primarily due to two key factors: higher leading gains and greater volume forcing. First, leading gains in these cavities are higher due to excitation of first depthwise

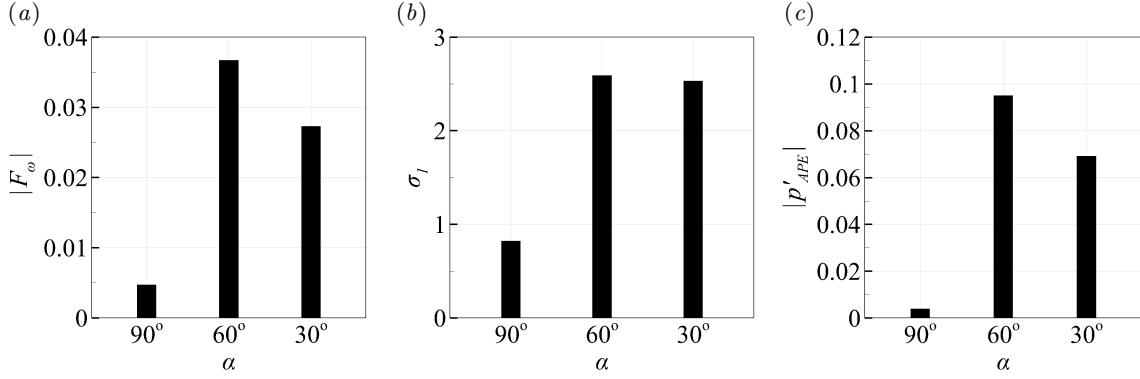


FIG. 21. (a) The magnitude of the integrated volume forcing, represented $|F_\omega|$, and (b) The first leading gain, denoted σ_1 , of the acoustic input-output operator. (c) The reconstructed acoustic response measured at the cavity base, $|p'_{APE}|$, obtained from the rank-1 approximation computed using Eq. (33).

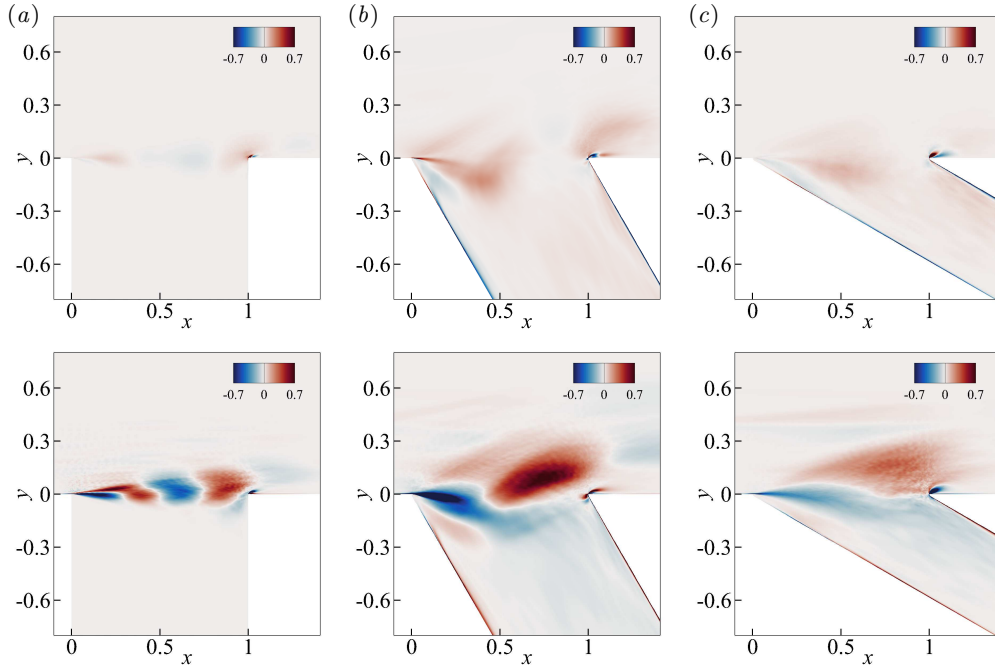


FIG. 22. The spatial distribution of the real part of the componentwise multiplication between the leading optimal forcing mode, v_1 , and the input forcing, \hat{f}_ω , in the (top row of the contour plots) streamwise direction and the (bottom row of the contour plots) vertical direction for cavities with inclinations of (a) $\alpha = 90^\circ$, (b) $\alpha = 60^\circ$, and (c) $\alpha = 30^\circ$, respectively. Note that the phase of the cycle, as shown in the contour plots, is selected such that the imaginary part of the integrated volume forcing is zero, to accentuate the source-sink cancellation effect.

acoustic modes, which exhibit minimal radiation losses and thus promote greater acoustic amplification, as illustrated in figure 21(b). Second, inclined cavities experience greater integrated-volume forcing due to reduced source-sink cancellation from the first hydrodynamic mode with a larger wavelength, as shown in figure 22(b,c). Ultimately, these critical factors contribute to the intensified acoustic responses observed in inclined cavities, as depicted in figure 21(c). Here, the acoustic input-output analysis proves useful in elucidating the physical mechanisms underpinning the results from inclined cavities at $M_\infty = 0.3$, which achieves the primary objective of this study.

Lastly, the discussions have primarily focused on elucidating the aeroacoustic characteristics of cavity oscillations, with limited attention given to the influence of incoming flow properties. To address this, we utilized insights from the acoustic particle velocity analysis for different pulsation levels, as discussed in Section III, to assess the impact of acoustic forcing near the upstream corner of the cavity on the cavity oscillation frequency. Here, the impact of the acoustic forcing is quantified by evaluating the peak acoustic particle displacement resulting from the depthwise

acoustic resonance, given by

$$\theta_a = \frac{|\hat{p}|}{\rho_\infty a_\infty He}, \quad (34)$$

where $|\hat{p}|$ represents the magnitude of the Fourier-transformed pressure fluctuations measured at the cavity base, and He denotes the peak Helmholtz number observed in the pressure spectra of the LES results. According to Bagwell [86], lock-in oscillation requires an acoustic particle displacement comparable to the momentum thickness. To test this criterion, we compared our LES data with previous experimental findings on deep cavity flows.

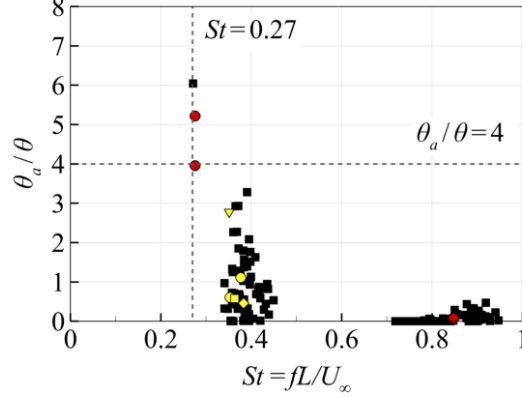


FIG. 23. The scatter plot shows the ratio of acoustic particle displacement θ_a to the momentum thickness θ at three distinct flow-acoustic resonance regimes. Different symbols represent data from various studies: (■) Yang et al. [9], (▼) Bagwell [86], (■) Forestier et al. [87], (◆) Ho and Kim [23], and the current LES results for (●) $M_\infty = 0.2$ and (●) $M_\infty = 0.3$. The horizontal line suggests that a critical ratio of $|\theta_a|/\theta \geq 4$ is required to excite the amplified resonance at $St \approx 0.27$.

Figure 23 illustrates the ratio of acoustic particle displacement to momentum thickness across three distinct flow-acoustic resonance regimes. The flow-acoustic resonance in the current orthogonal cavity case at $M_\infty = 0.3$ resides in the third resonance regime (i.e., $St \approx 0.85$), corresponding to the second hydrodynamic mode, and has a small ratio of acoustic particle displacement to momentum thickness. Conversely, none of the oscillations in inclined cavities at $M_\infty = 0.3$ correspond to the second interval ($St \approx 0.385$), which is associated with the first hydrodynamic mode. Interestingly, experimental studies by Yang et al. [9] in orthogonal deep cavities have identified an unexpected and strong cavity resonance mode, termed as “ $h1^*a1$ ”, occurring at a lower frequency of $St \approx 0.27$. This Strouhal number coincides closely with the frequency of the inclined cavities at $M_\infty = 0.3$, suggesting that such flow-acoustic resonances are prominent when the ratio of acoustic particle displacement to momentum thickness surpasses a certain minimum threshold. Based on these observations, we suggest that the intense flow-acoustic resonances at $St \approx 0.27$ could be linked to a nonlinearly shifted first hydrodynamic mode, facilitated by large shear-layer oscillations when the ratio of acoustic particle displacement to momentum thickness exceeds $|\theta_a|/\theta \geq 4$.

VI. CONCLUDING REMARKS

In this paper, we have investigated the aeroacoustic responses of deep cavities with an aspect ratio of $D/L = 2.632$ subjected to two Mach numbers of 0.2 and 0.3 at three different inclination angles ($\alpha = 30^\circ$, 60° , and 90°) using wall-resolved large-eddy simulations. The numerical results revealed that the inclined cavities at $M_\infty = 0.3$ unexpectedly generated acoustic responses with peak amplitudes nearly 30 dB higher than those observed in the orthogonal cavity case. Furthermore, the peak frequency (i.e., $St \approx 0.27$) was significantly lower compared to those of the orthogonal cases. We performed various analysis techniques to investigate the physical mechanisms underpinning these distinct aeroacoustic behaviors. For the orthogonal cavity, we demonstrated that the self-sustained oscillations are caused by a lock-in event between the second hydrodynamic mode (i.e., $St \approx 0.85$) and the third depthwise acoustic mode (i.e., $He \approx 0.255$), where the latter acoustic mode exhibited significant radiation losses. In contrast, the inclined cavities exhibited intensified oscillations that stemmed from lock-ins between the nonlinearly shifted first hydrodynamic mode (i.e., $St \approx 0.27$) and the first depthwise acoustic mode (i.e., $He \approx 0.083$). This hydrodynamic mode was associated with large shear-layer oscillations that forced the trajectory of the main vortex submerged deep into the cavity where the mean flow was slower. Consequently, the vortex experienced a longer travel time per cycle compared to the

orthogonal cavity case, resulting in a slower vortex convection speed and a lower peak frequency. Additionally, acoustic input-output analysis revealed higher amplification rates of the fundamental depthwise acoustic modes and reduced source-sink cancellations by the larger wavelength of the first hydrodynamic modes as key mechanisms contributing to the pronounced aeroacoustic responses in the inclined cavities. Finally, this paper suggested that the ratio between the acoustic particle displacement and the momentum thickness ($|\theta_a|/\theta$) may be used as a criterion to predict the onset of the distinctive resonance and discussed that the distinctive resonance frequency (i.e., $St \approx 0.27$), shifted from the first hydrodynamic mode frequency due to the aforementioned nonlinear mechanisms, takes place when $|\theta_a|/\theta \geq 4$.

While the current study provides valuable insights into flow-acoustic resonances in deep and inclined cavity configurations, it has certain limitations that warrant further research. Firstly, the current findings are limited to the specific aspect ratio of $L/D = 2.632$ and the Mach numbers of 0.2 and 0.3 used in this study. Further studies are needed to explore a deeper understanding of the nonlinear mode shift mechanisms at different aspect ratios and a wider range of Mach and Reynolds numbers. Secondly, the study focused on a two-dimensional geometry, and the effects of three-dimensional geometries, such as rectangular or circular cross-sections of the cavity, with inclinations require further investigation. Also, different cavity floor orientations (e.g., non-orthogonal to the side walls) might have impacts on the resonance frequency and amplitude. Finally, future research should explore potential mitigation or control methods to reduce the resonance noise generated by deep and inclined cavities, as this phenomenon can have significant practical implications in various engineering applications.

ACKNOWLEDGMENTS

The authors would like to acknowledge the studentship provided by Rolls-Royce UTC (University Technology Centre) for Propulsion Systems Noise at the University of Southampton. The authors also thank EPSRC (Engineering and Physical Sciences Research Council) for the computational time made available on the UK supercomputing facility ARCHER2 via the UK Turbulence Consortium (EP/R029326/1).

-
- [1] J. T. Coffman and M. D. Bernstein, Failure of safety valves due to flow-induced vibration, *Journal of Pressure Vessel Technology* **102**, 112 (1980).
 - [2] D. Galbally, G. García, J. Hernando, J. de Dios Sánchez, and M. Barral, Analysis of pressure oscillations and safety relief valve vibrations in the main steam system of a boiling water reactor, *Nuclear Engineering and Design* **293**, 258 (2015).
 - [3] J. C. Bruggeman, A. Hirschberg, M. E. H. van Dongen, A. P. J. Wijnands, and J. Gorter, Flow induced pulsations in gas transport systems: Analysis of the influence of closed side branches, *Journal of Fluids Engineering* **111**, 484 (1989).
 - [4] S. Ziada, Flow-excited acoustic resonance in industry, *Journal of Pressure Vessel Technology* **132** (2010).
 - [5] S. Ziada, A. Oengören, and A. Vogel, Acoustic resonance in the inlet scroll of a turbo-compressor, *Journal of Fluids and structures* **16**, 361 (2002).
 - [6] A. A. Aleksentsev, A. N. Sazhenkov, and S. V. Sukhinin, Acoustic resonance phenomena in air bleed channels in aviation engines, *Journal of Applied Mechanics and Technical Physics* **57**, 971 (2016).
 - [7] C. Perrot-Minot, E. Mignot, R. Perkins, D. Lopez, and N. Riviere, Vortex shedding frequency in open-channel lateral cavity, *Journal of Fluid Mechanics* **892** (2020).
 - [8] M. C. A. M. Peters, *Aeroacoustic sources in internal flows* (Eindhoven University of Technology, 1993).
 - [9] Y. Yang, D. Rockwell, K. L. F. Cody, and M. Pollack, Generation of tones due to flow past a deep cavity: Effect of streamwise length, *Journal of Fluids and Structures* **25**, 364 (2009).
 - [10] J. E. Rossiter, *Wind tunnel experiments on the flow over rectangular cavities at subsonic and transonic speeds*, Tech. Rep. (Ministry of Aviation; Royal Aircraft Establishment; RAE Farnborough, 1964).
 - [11] C. W. Rowley and D. R. Williams, Dynamics and control of high-reynolds-number flow over open cavities, *Annu. Rev. Fluid Mech.* **38**, 251 (2006).
 - [12] K. Karamcheti, Acoustic radiation from two-dimensional rectangular cut-outs in aerodynamic surfaces, *NACA TN* **3487** (1955).
 - [13] H. E. Plumblee, J. S. Gibson, and L. W. Lassiter, *A theoretical and experimental investigation of the acoustic response of cavities in an aerodynamic flow*, Tech. Rep. (Lockheed Aircraft Corp Marietta GA, 1962).
 - [14] L. F. East, Aerodynamically induced resonance in rectangular cavities, *Journal of Sound and Vibration* **3**, 277 (1966).
 - [15] D. Rockwell and E. Naudascher, Review—self-sustaining oscillations of flow past cavities, *Journal of Fluids Engineering* **100**, 152 (1978).
 - [16] W. Koch, Acoustic resonances in rectangular open cavities, *AIAA Journal* **43**, 2342 (2005).
 - [17] C. K. W. Tam, Excitation of instability waves in a two-dimensional shear layer by sound, *Journal of Fluid Mechanics* **89**, 357 (1978).
 - [18] D. Tonon, A. Hirschberg, J. Golliard, and S. Ziada, Aeroacoustics of pipe systems with closed branches, *International Journal of Aeroacoustics* **10**, 201 (2011).

- [19] S. Ziada and P. Lafon, Flow-excited acoustic resonance excitation mechanism, design guidelines, and counter measures, *Applied Mechanics Reviews* **66** (2014).
- [20] E. Tinar and D. Rockwell, Generation of locked-on flow tones: Effect of damping, *Journal of Fluids and Structures* **44**, 129 (2014).
- [21] C. W. Rowley, T. Colonius, and A. J. Basu, On self-sustained oscillations in two-dimensional compressible flow over rectangular cavities, *Journal of Fluid Mechanics* **455**, 315 (2002).
- [22] B. A. Tuna and D. Rockwell, Self-sustained oscillations of shallow flow past sequential cavities, *Journal of Fluid Mechanics* **758**, 655 (2014).
- [23] Y. W. Ho and J. W. Kim, A wall-resolved large-eddy simulation of deep cavity flow in acoustic resonance, *Journal of Fluid Mechanics* **917** (2021).
- [24] S. Ziada, A flow visualization study of flow-acoustic coupling at the mouth of a resonant side-branch, *Journal of Fluids and Structures* **8**, 391 (1994).
- [25] S. Dequand, S. Hulshoff, and A. Hirschberg, Self-sustained oscillations in a closed side branch system, *Journal of Sound and Vibration* **265**, 359 (2003).
- [26] R. Bravo, S. Ziada, and M. Dokainish, Aeroacoustic response of an annular duct with coaxial closed side branches, in *11th AIAA/CEAS Aeroacoustics Conference* (2005) p. 3019.
- [27] V. Theofilis, Globally unstable basic flows in open cavities, in *6th Aeroacoustics Conference and Exhibit* (2000) p. 1965.
- [28] F. Giannetti and P. Luchini, Structural sensitivity of the first instability of the cylinder wake, *Journal of Fluid Mechanics* **581**, 167 (2007).
- [29] G. A. Bres and T. Colonius, Three-dimensional instabilities in compressible flow over open cavities, *Journal of Fluid Mechanics* **599**, 309 (2008).
- [30] V. Theofilis, Global linear instability, *Annual Review of Fluid Mechanics* **43**, 319 (2011).
- [31] S. Yamouni, D. Sipp, and L. Jacquin, Interaction between feedback aeroacoustic and acoustic resonance mechanisms in a cavity flow: a global stability analysis, *Journal of Fluid Mechanics* **717**, 134 (2013).
- [32] P. J. Schmid and L. Brandt, Analysis of Fluid Systems: Stability, Receptivity, Sensitivity: Lecture notes from the FLOW-NORDITA Summer School on Advanced Instability Methods for Complex Flows, Stockholm, Sweden, 2013, *Applied Mechanics Reviews* **66** (2014), 024803.
- [33] F. Meseguer-Garrido, J. D. Vicente, E. Valero, and V. Theofilis, On linear instability mechanisms in incompressible open cavity flow, *Journal of Fluid Mechanics* **752**, 219 (2014).
- [34] V. Citro, F. Giannetti, L. Brandt, and P. Luchini, Linear three-dimensional global and asymptotic stability analysis of incompressible open cavity flow, *Journal of Fluid Mechanics* **768**, 113 (2015).
- [35] Q. Liu, F. Gómez, and V. Theofilis, Linear instability analysis of low-incompressible flow over a long rectangular finite-span open cavity, *Journal of Fluid Mechanics* **799**, R2 (2016).
- [36] Y. Sun, K. Taira, L. N. Cattafesta, and L. S. Ukeiley, Biglobal instabilities of compressible open-cavity flows, *Journal of Fluid Mechanics* **826**, 270 (2017).
- [37] J. M. Chomaz, Global instabilities in spatially developing flows: non-normality and nonlinearity, *Annu. Rev. Fluid Mech.* **37**, 357 (2005).
- [38] O. Marquet and L. Lesshafft, Identifying the active flow regions that drive linear and nonlinear instabilities, *arXiv preprint arXiv:1508.07620* (2015).
- [39] L. N. Trefethen, A. E. Trefethen, S. C. Reddy, and T. A. Driscoll, Hydrodynamic stability without eigenvalues, *Science* **261**, 578 (1993).
- [40] B. J. McKeon and A. S. Sharma, A critical-layer framework for turbulent pipe flow, *Journal of Fluid Mechanics* **658**, 336 (2010).
- [41] Y. Sun, Q. Liu, L. N. Cattafesta III, L. S. Ukeiley, and K. Taira, Resolvent analysis of compressible laminar and turbulent cavity flows, *AIAA journal* **58**, 1046 (2020).
- [42] Q. Liu, Y. Sun, C.-A. Yeh, L. S. Ukeiley, L. N. Cattafesta, and K. Taira, Unsteady control of supersonic turbulent cavity flow based on resolvent analysis, *Journal of Fluid Mechanics* **925** (2021).
- [43] E. Boujo, M. Bauerheim, and N. Noiray, Saturation of a turbulent mixing layer over a cavity: response to harmonic forcing around mean flows, *Journal of Fluid Mechanics* **853**, 386 (2018).
- [44] L. Larchevêque, P. Sagaut, I. Mary, O. Labbé, and P. Comte, Large-eddy simulation of a compressible flow past a deep cavity, *Physics of Fluids* **15**, 193 (2003).
- [45] B. Thornber and D. Drikakis, Implicit large-eddy simulation of a deep cavity using high-resolution methods, *AIAA journal* **46**, 2634 (2008).
- [46] P. Sampath and K. P. Sinhamahapatra, Numerical analysis of characteristic features of shallow and deep cavity in supersonic flow, *International Journal of Computational Fluid Dynamics* **30**, 231 (2016).
- [47] Z. Chen and N. A. Adams, Mode interactions of a high-subsonic deep cavity, *Physics of Fluids* **29** (2017).
- [48] T. Pedergnana, C. Bourquard, A. Faure-Beaulieu, and N. Noiray, Modeling the nonlinear aeroacoustic response of a harmonically forced side branch aperture under turbulent grazing flow, *Physical Review Fluids* **6**, 023903 (2021).
- [49] J. W. Kim, High-order compact filters with variable cut-off wavenumber and stable boundary treatment, *Comput. Fluids* **39**, 1168 (2010).
- [50] D. J. Garmann, M. R. Visbal, and P. D. Orkwis, Comparative study of implicit and subgrid-scale model large-eddy simulation techniques for low-reynolds number airfoil applications, *International Journal for Numerical Methods in Fluids* **71**, 1546 (2012).
- [51] F. M. White, *Viscous fluid flow* 2nd edition mcgraw-hill, New York (1991).

- [52] J. W. Kim and P. J. Morris, Computation of subsonic inviscid flow past a cone using high-order schemes, *AIAA J.* **40**, 1961 (2002).
- [53] J. W. Kim, A. S. H. Lau, and N. D. Sandham, CAA boundary conditions for airfoil noise due to high-frequency gusts, *Proc. Eng.* **6**, 244 (2010).
- [54] J. W. Kim, A. S. H. Lau, and N. D. Sandham, Proposed boundary conditions for gust-airfoil interaction noise, *AIAA J.* **48**, 2705 (2010).
- [55] J. W. Kim, Optimised boundary compact finite difference schemes for computational aeroacoustics, *J. Comput. Phys.* **225**, 995 (2007).
- [56] J. W. Kim and D. J. Lee, Generalized characteristic boundary conditions for computational aeroacoustics, *AIAA J.* **38**, 2040 (2000).
- [57] J. W. Kim and D. J. Lee, Generalized characteristic boundary conditions for computational aeroacoustics, part 2, *AIAA J.* **42**, 47 (2004).
- [58] J. W. Kim, Quasi-disjoint pentadiagonal matrix systems for the parallelization of compact finite-difference schemes and filters, *J. Comput. Phys.* **241**, 168 (2013).
- [59] T. Y. Na and Y. P. Lu, Turbulent flow development characteristics in channel inlets, *Applied Scientific Research* **27**, 425 (1973).
- [60] D. B. Spalding, A single formula for the “law of the wall”, *Journal of Applied Mechanics* **28**, 455 (1961).
- [61] A. Lozano-Durán and J. Jiménez, Effect of the computational domain on direct simulations of turbulent channels up to $Re_\tau = 4200$, *Physics of Fluids* **26** (2014).
- [62] M. E. Goldstein, *Aeroacoustics* (McGraw-Hill, 1976) pp. 54–59.
- [63] R. Ewert and W. Schröder, Acoustic perturbation equations based on flow decomposition via source filtering, *Journal of Computational Physics* **188**, 365 (2003).
- [64] K. Aly and S. Ziada, Effect of mean flow on the trapped modes of internal cavities, *Journal of Fluids and Structures* **33**, 70 (2012).
- [65] N. Arya and A. De, Effect of vortex and entropy sources in sound generation for compressible cavity flow, *Physics of Fluids* **33**, 046107 (2021).
- [66] K. W. Thompson, Time dependent boundary conditions for hyperbolic systems, *Journal of Computational Physics* **68**, 1 (1987).
- [67] K. W. Thompson, Time-dependent boundary conditions for hyperbolic systems, II, *Journal of Computational Physics* **89**, 439 (1990).
- [68] G. W. Stewart, A krylov–schur algorithm for large eigenproblems, *SIAM Journal on Matrix Analysis and Applications* **23**, 601 (2002).
- [69] P. E. Doak, Momentum potential theory of energy flux carried by momentum fluctuations, *Journal of Sound and Vibration* **131**, 67 (1989).
- [70] S. Unnikrishnan and D. V. Gaitonde, Acoustic, hydrodynamic and thermal modes in a supersonic cold jet, *Journal of Fluid Mechanics* **800**, 387 (2016).
- [71] S. Unnikrishnan and D. V. Gaitonde, A pressure decomposition framework for aeroacoustic analysis of turbulent jets, *European Journal of Mechanics - B/Fluids* **81**, 41 (2020).
- [72] S. W. Rienstra, *Fundamentals of duct acoustics*, Von Karman Institute Lecture Notes (2015).
- [73] J. Bruggeman, *Flow induced pulsations in pipe systems*, Ph.D. thesis, Department of Applied Physics (1987).
- [74] P. Bradshaw, A note on poisson’s equation for pressure in a turbulent flow, *Physics of Fluids* **24**, 777 (1981).
- [75] A. M. Naguib and M. M. Koochesfahani, On wall-pressure sources associated with the unsteady separation in a vortex-ring/wall interaction, *Physics of Fluids* **16**, 2613 (2004).
- [76] N. Curle, The influence of solid boundaries upon aerodynamic sound, *Proceedings of the Royal Society of London. Series A. Mathematical and Physical Sciences* **231**, 505 (1955).
- [77] J. Larsson, L. Davidson, M. Olsson, and L. Eriksson, Aeroacoustic investigation of an open cavity at low mach number, *AIAA journal* **42**, 2462 (2004).
- [78] G. Lam, R. Leung, and S. Tang, Aeroacoustics of t-junction merging flow, *The Journal of the Acoustical Society of America* **133**, 697 (2013).
- [79] Y. P. Tang and D. Rockwell, Instantaneous pressure fields at a corner associated with vortex impingement, *Journal of Fluid Mechanics* **126**, 187 (1983).
- [80] G. Haller and G. Yuan, Lagrangian coherent structures and mixing in two-dimensional turbulence, *Physica D: Nonlinear Phenomena* **147**, 352 (2000).
- [81] M. Green, C. Rowley, and G. Haller, Detection of lagrangian coherent structures in 3d turbulence, *Journal of Fluid Mechanics* **18547**, 20 (2006).
- [82] P. C. Kriesels, M. C. A. M. Peters, A. Hirschberg, A. P. J. Wijnands, A. Iafrafi, G. Riccardi, R. Piva, and J. C. Bruggeman, High amplitude vortex-induced pulsations in a gas transport system, *Journal of Sound and Vibration* **184**, 343 (1995).
- [83] D. Rockwell and E. Naudascher, Self-sustained oscillations of impinging free shear layers, *Annual Review of Fluid Mechanics* **11**, 67 (1979).
- [84] M. S. Howe, *Acoustics of fluid-structure interactions* (Cambridge University Press, 1998).
- [85] M. S. Howe, *Theory of Vortex Sound*, Cambridge Texts in Applied Mathematics (Cambridge University Press, 2003).
- [86] T. G. Bagwell, CFD simulation of flow tones from grazing flow past a deep cavity (2006) pp. 105–114.
- [87] N. Forestier, L. Jacquin, and P. Geffroy, The mixing layer over a deep cavity at high-subsonic speed, *Journal of Fluid Mechanics* **475**, 101 (2003).